Poly ADP-ribosylation of SET8 leads to aberrant H4K20me1 domains in mammalian cells

Pierre-Olivier Estève *, Vishnu US*, Cristian Ruse, Hang Gyeong Chin and Sriharsa Pradhan**

New England Biolabs Inc, 240 County Road, Ipswich, MA 01938, USA

* Equal contribution to the work.

**Correspondence:

Sriharsa Pradhan, Ph.D.

New England Biolabs

Ipswich, MA 01983, USA

e-mail: pradhan@neb.com

Phone: (978) 380-7227

FAX: (978) 921-1350

Abstract

In mammalian cells, SET8 mediated Histone H4 Lys 20 monomethylation (H4K20me1) has been implicated in regulating mitotic condensation, DNA replication, DNA damage response, and gene expression. Here we show SET8, the only known enzyme for H4K20me1 is post-translationally poly ADP-ribosylated by PARP1 on lysine residues. PARP1 interacts with SET8 in a cell cycle- dependent manner. Poly ADP-ribosylation on SET8 renders it catalytically compromised and it undergoes degradation via ubiquitylation pathway. Knockdown of PARP1 shifted the relative dynamic equilibrium of H4K20me2 to H4k20me3 in cells. Overexpression or knockdown of PARP1 led to aberrant H4K20me1 domains genome-wide, impacting Wnt signaling pathways genes and transcription factor binding site enrichment. Therefore, SET8 mediated chromatin remodeling and gene expression in mammalian cells are influenced by poly ADP-ribosylation by PARP1.

Introduction

In the eukaryotic nucleus, double-stranded DNA is wrapped around histone octamers to make chromatin fibers. These chromatin fibers undergo various structural changes during cell division and organism development (1-3). The decompaction and re-establishment of chromatin organization immediately after mitosis are essential for genome regulation (4). Given the absence of membranes separating intranuclear substructures and during cell division, it has been postulated that other structural features of the nucleus, such as the chromatin itself, must impart regulations that would control molecular information flow and stage different physiological activities. Indeed, chromatin accessibility plays a central role in ensuring cell cycle exit and the terminal differentiation during metamorphosis (5). Furthermore, chromatin compaction threshold in cells exiting mitosis ensures genome integrity by limiting replication licensing in G1 phase. Recent studies on histone writer enzymes have shade some lights on the role of histone marks in cell biology (6). The nucleosome structure illustrates that highly basic histone amino (N)-terminal tails can protrude from the core and would be in direct contact with adjacent nucleosomes. Therefore, modification of these histone tails would affect inter-nucleosomal interactions, and thus would modulate the overall chromatin 3D-structure and compaction. Recent advances in Hi-C studies support that this is indeed the case, where transcriptionally active A and inactive B compartments are differentially positioned in the nucleus (7). Histone modifications not only regulate chromatin structure by merely being there, but they also recruit chromatin readers and remodeling enzymes that utilizes the energy derived from the hydrolysis of ATP to reposition nucleosomes (6). For example, lysine acetylation of histone tails is dynamic and regulated by the opposing action of two families of enzymes, histone acetyltransferases (HATs) for acetylation, and histone deacetylases (HDACs) to remove the acetyl group (8). Indeed, acetylated histones on the chromatin are a cue to transcriptional gene activation (9). Therefore, the balancing act between both HATs and HDACs is essential in maintaining the dynamic equilibrium during gene expression.

The other significant chromatin mark, histone methylation, primarily occurs on the side chains of lysines and arginines (10). Histone methylation does not alter the charge of the histone protein, unlike phosphorylation. However, the epsilon amino group of lysines may be modified to mono-, di- or tri-methylated configuration, whereas arginine may be mono-, symmetrically or asymmetrically di-methylated, creating an unprecedented array of complexity for the reader proteins. These core modifications are established and propagated by SET domain containing enzymes (11). One such enzyme is SET8 (also known as KMT5A, PR-Set7 and SETD8), the only histone methyltransferase that monomethylates histone H4K20 (H4K20me1) (12,13). Subsequent modification of H4K20me1 by Suv4-20h1/h2 leads to the transition from H4K20me1 to H4K20me2/3 (14). Although H4K20 specific demethylases are less understood, PHF8 is the only known enzyme that demethylates H4K20me1 to H4K20 (15). Similarly, Rad23

has also been shown to demethylate H4K20me1/2/3 (16). In the mouse genome, H4K20 methylation state is distributed in specific regions and is bound by specific reader proteins. Histone H4K20me1 has been implicated in regulating diverse processes ranging from the DNA damage response, mitotic condensation, DNA replication and gene regulation. Indeed, loss of the SET8 causes a more severe and complex phenotype, as this negates the catalysis of all levels of H4K20 methylation. Loss of SET8 causes lethality at the third instar larval stage in Drosophila (17), and in mice it leads to embryonic lethality via developmental arrest between the four- and eight-cell stages (12). Rescue experiments on mouse SET8-/- phenotype embryos by reintroduction of either catalytically active or inactive allele have demonstrated that the catalytic activity of the enzyme is essential for embryo development.

SET8 protein expression is tightly regulated during the cell cycle; it is highest during G2/M and early G1 and is absent during the S phase. Indeed, upon mitotic exit, chromatin relaxation is controlled by SET8-dependent methylation of histone H4K20. In the absence of either SET8 or H4K20me1, substantial genome-wide chromatin decompaction occurs allowing excessive loading of the origin recognition complex (ORC) in the daughter cells (18). During cell cycle, SET8 undergoes ubiquitination and phosphorylation. SET8 is a direct substrate of the E3 ubiquitin ligase complex CRL4Cdt2 (19-21). In addition, SET8 is also regulated by the E3 ubiquitin ligase SCF/Skp2 (22). Skp2 degrades substrates during S and G2 phase and may partially contribute to the steep decrease in SET8 levels during the S phase (23). The other post-translational modification of SET8 that may affect its activity or stability is serine phosphorylation, as discovered by proteomics studies (24-26). SET8 S29 is phosphorylated in vivo by Cyclin B/cdk1 during mitosis, and it causes SET8 to dissociate from mitotic chromosomes at anaphase and relocate to the extrachromosomal space, where it is dephosphorylated by cdc14 phosphatase and subsequently subjected to ubiquitination by APC/Cdh1 (27). Therefore, the coordination of ubiquitylation and phosphorylation processes may be necessary to maintain precise levels of H4K20me1 and SET8 in the genome.

Apart from acetylation, methylation, phosphorylation, and ubiquitylation, poly ADP-ribosylation is another post-translational modification of proteins catalyzed by PARP family of enzymes by the addition of linear or branched chains of ADP-ribose units, from NAD+ substrate (28). The central enzyme for poly ADP-ribosylation in cells during DNA damage is poly-ADP-ribose polymerase 1 (PARP1). Multiple different amino acids are shown to be acceptors of PAR, such as Lys, Arg, Glu, Asp, Cys, Ser, Thr, pSer (phospho-serine, through the phosphate group), although His and Tyr residues were also proposed by proteomic approaches (29-35). PARP family members modify many proteins by poly and/or mono ADP-ribosylation (36). PARPs catalyze short or long, branched, or linear ribosylation. The structural diversity of poly ADP-

ribosylation on these proteins could be recognized by poly ADP-ribosylation readers (or binders) with their specific binding motifs for biological function.

In a proteomics study of SET8 binding proteins, we found PARP1 as a strong binder (Table S1). This led us to study the nature of SET8-PARP1 interaction and the role of poly ADP-ribosylation on the catalytic activity of enzymes. Here, we have also investigated the role of poly ADP-ribosylation in SET8 degradation, chromatin remodeling and gene expression in mammalian cells.

Materials and Methods

Cell culture, transfections, and cell cycle synchronization: HeLa, HCT116 and COS-7 cells were cultured in DMEM supplemented with 10% fetal bovine serum according to ATCC's recommendations. For PARP1 overexpression, HeLa cells were transfected with 500 ng of 3xFLAG or 3xFLAG-PARP1 plasmids using Fugene HD transfection reagent (Promega, # E2311) according to manufacturer's recommendations. Cells were harvested after 48 hrs. For PARP1 and SET8 knockdown, HeLa cells were transfected with 10 nM of esiRNA targeting either PARP1 (Millipore-Sigma # EHU050101) or SET8 (Millipore-Sigma # EHU111111) using HiPerfect reagent according to manufacturer's protocol (Qiagen # 301704). 10 nM of esiRNA against EGFP (Millipore-Sigma # EHUEGFP) was used as control and cells were harvested after 48 hrs.

For cell cycle studies, HeLa cells were synchronized using 2 mM thymidine for 24 hrs, washed once with media and released for 8 hours with 24 mM dCTP (New England Biolabs # N0441S). 2 mM of thymidine or 0.1 mg/ml of Nocodazole (Millipore-Sigma # SML1665) were added for 14-15 hrs to arrest the cells in S or G2/M phase respectively. Chromatin was extracted using CSK buffer (10 mM Pipes pH 6.8, 300 mM sucrose, 100 mM NaCl, 1.5 mM MgCl2 and 0.5% Triton X-100 supplemented with protease cocktail inhibitors and PMSF) for 30 min on ice. Cells were centrifuged at 2,000 g at 4°C for 5 min, washed once with CSK buffer and the pellet (chromatin) was resuspended in buffer containing 50 mM Tris.Cl, pH 7.5, 200 mM NaCl and 1% SDS. Chromatin was then sonicated (10 cycles of 10 pulses) and used either as total chromatin extract or SET8 immunoprecipitation.

Western Blot and Densitometry: Western blots were performed as previously described (37). Antibodies against SET8 were obtained from Cell Signaling Technology (# 2996), ABCAM (# ab3798) and Santa Cruz Biotechnology (# sc-515433). Anti-PARP1 (# 9532) and anti-ADPribose antibody (# 83732S) were purchased from Cell Signaling Technology. Anti-H4K20me1 (# MA5-18067), anti-histone H4K20me2 (# 9759) and anti-H4K20me3 (# 5737) were obtained from Thermo Fisher Scientific and Cell Signaling Technology respectively and used at 1/1000 dilution. Anti-β-actin (# 4970S) and anti-GFP (# 11814460001) antibodies were obtained from Cell Signaling Technology and Millipore-Sigma respectively and used at a 1:5000 dilution. Densitometry was performed using ImageJ software (W. S. Rasband, National Institutes of Health). All densitometry values (arbitrary units) were normalized to either their respective β-actin or Ponceau S staining.

In vivo Ubiquitination Assay: COS-7 cells were co-transfected with a mixture of GFP or GFP-SET8, 3xFLAG or 3xFLAG-PARP1, HA-ubiquitin plasmids, and Fugene HD transfection reagent (Promega, # E2311) according to manufacturer's recommendations. After 48 hrs, transfected COS-7 cells were treated or not with 50 µM MG132 for 2 h and lysed as described previously

(38). Cell lysates (100–200 µg) were then immunoprecipitated with GFP antibody (Roche Applied Science). Ubiquitination was detected as described previously (38).

PARP1 and SET8 cloning and mutagenesis: Sequences coding for PARP1 full-length (cDNA obtained from Origen # RC20708), SET8 full-length (39) were cloned into pEGFP-C2 or pGEX5X.1 vector and transformed into NEB 10-beta competent E.Coli (New England Biolabs # C3019H). Mutagenesis to generate PARP1, SET8 domains as well as point mutations were performed using Q5 site-directed mutagenesis kit (New England Biolabs # E0554S). Primers used for cloning and mutagenesis are available upon request.

PARP1 and SET8 interaction studies: For *in vitro* interaction studies, PARP1 and SET8 GST-fusion and mutant proteins were induced in Escherichia coli ER2566 cells (New England Biolabs # C2566H) using 0.4mM IPTG overnight at 16°C. Purification of recombinant fusion proteins from the bacterial lysate were performed as previously described (40). For GST pull-down assay, GST or the GST fusion proteins was bound to glutathione-Sepharose beads. The assay was performed by pre-incubating the GST or GST fusion protein beads with 100 µg/ml bovine serum albumin (BSA) and the protein to be studied in a binding buffer (1X PBS with 0.1% Triton X-100) with end over end mixing at 4°C for 1 h. Beads were washed 3 times for 5 min with a binding buffer containing 1% Triton X-100. The beads were mixed with 1× SDS–PAGE sample loading buffer (New England Biolabs # B7703S) and incubated at 98°C for 5 min. The protein mixtures were separated on a 10% polyacrylamide Tricine gel (Thermo Fisher Scientific # EC6675BOX). Recombinant PARP1 was purchased from Active Motif (# 81037), SET8 was purified from New England Biolabs (# M0428).

Co-immunoprecipitation of endogenous PARP1 and SET8 were performed with 200 µg of total extract from crosslinked HCT116 or HeLa cells with 1% formaldehyde for 10 min using anti-PARP1 antibody (Cell Signaling Technology # 9532), anti-SET8 antibody (Santa Cruz Biotechnology # sc-515433) or 5 µg of rabbit IgG as a control antibody (Santa Cruz Biotechnology # sc-2027). The immunoprecipitations (IP) were performed overnight with end-over-end mixing at 4°C in TD buffer (50 mM HEPES, pH 7.5, 250 mM NaCl and 1% Triton X-100). The antibodies were captured using 50 µl of protein G magnetic beads (S1430, New England Biolabs) incubated for 60 min with end over end mixing at 4°C. After 3 washes with TD buffer, IP reactions were blotted using anti-PARP1 antibody (Millipore-Sigma # HPA045168) and rabbit anti-SET8 antibody (Cell Signaling Technology # 2996S). For immunoprecipitation of SET8 from synchronized HeLa cells, 200 µg of chromatin cell lysate was incubated with 5 µg of anti-SET8 (sc-515433, Santa Cruz). IP reactions were performed and blotted with anti-PARP1 and anti-SET8 antibodies as described above.

Immunofluorescence studies: For the detection of PARP1 and SET8 colocalization, COS-7 cells were grown on coverslips and co-transfected with FLAG-PARP1 and GFP-SET8 plasmids as described above. After 48 hrs, cells were crosslinked with 4% paraformaldehyde (Electron Microscopy Sciences # 15710) for 10 min at RT and quenched with 0.125M Glycine for 5 min at RT. After 20 min permeabilization with 100 % methanol for 20 min at -20°C, cells were incubated with PBS including 0.5 % Tween20 and 5% BSA (Millipore-Sigma # A-7906) for 1 hr at RT. Epitope tagged PARP1 was detected by mouse anti-FLAG antibody (# F3165, Millipore-Sigma) and visualized with an anti-mouse IgG coupled with Alexa Fluor 594 dye (Thermo Fisher Scientific # A-11005). GFP-SET8 and FLAG-PARP1 were detected using 458, 488, 514 nm multiline Argon laser and 561 nm DPSS laser, respectively. Endogenous PCNA was visualized with anti-PCNA Alexa Fluor 647 conjugate (Cell Signaling Technology #82968S) using 633 nm HeNe laser. Slides were mounted using Prolong Gold Antifade Mountant with DAPI (Thermo Fisher Scientific # P36931). Images were captured using a confocal microscope (LSM 880, Zeiss).

DNA replication sites were detected using EDU Staining Proliferation Kit (iFluor 647, ABCAM # ab222421) on GFP-SET8 full-length transfected COS-7 cells according to manufacturer's recommendations. Before EDU labeling, GFP-SET8 transfected COS-7 cells were pretreated with 20 µM of PARG inhibitor (Millipore-Sigma # SML1781) for 1 hr. After EDU labeling, cells were incubated overnight at 4C with anti-pan-ADPribose reagent at 1/400 dilution (Millipore-Sigma # MABE1016). ADPribose was detected using anti-rabbit IgG coupled with Alexa Fluor 594 dye (Thermo Fisher Scientific # A32740). EDU was visualized using 633 nm HeNe laser. Slides were mounted and images were captured as described above.

SET8 gel shift DNA-nucleosome binding assays: For SET8 DNA gel shift assay, Cy3-end-labeled EcoRI hairpin oligonucleotide (0.5 µM) (GG<u>GAATTC</u>CCAAAGG<u>GAATTC</u>CC, EcoRI sites underlined) and different concentration of recombinant His-SET8 protein (0 to 1.4 µM, New England Biolabs) were incubated for 10 min on ice in 1× GRB binding buffer [20 mM HEPES pH 7.5, 10% glycerol, 25 mM KCl, 0.1 mM EDTA, 1 mM dithiothreitol (DTT), 2 mM MgCl2, 0.2% NP40] in a 20 µl reaction volume. Protein–DNA complexes were resolved on a 6% TBE DNA retardation gel (Thermo Fisher Scientific # EC6365BOX) at 4°C in 0.5× TBE (45 mM Tris–HCl, 45 mM H3BO3, 10 mM EDTA pH 8.3) at 140 V. Complex were visualized using Typhoon scanner. Kd was calculated using GraphPad Prism 8.0.

For GST-SET8 full-length as well as mutant DNA or nucleosome binding, 5 µg of GST-beads were incubated for 15 min on ice in GRB buffer in a 25 µl reaction volume with 1 µg of 100 bp DNA ladder (New England Biolabs # N3231S) or mononucleosome (Active motif # 81070). After 1,000 rpm spin for 5 min at 4°C, supernatant representing the unbound DNA was mixed with 6x purple dye (New England Biolabs # B7024S) and loaded on a 6% TBE DNA retardation gel

(Thermo Fisher Scientific # EC6365BOX) at 4°C in 0.5× TBE at 140 V. DNA was visualized under UV Transilluminator. In some cases, GST or GST-SET8 full-length fusion proteins were ADP-ribosylated using PARP1 recombinant enzyme (Active Motif # 81037) during 15 min at RT. The GST beads were then washed twice with PBS+1% Triton X-100 and 1M NaCl to remove PARP1 bound to the beads. After 2 other washes with 1X PBS containing 0.1% Triton X-100, beads were resuspended in GRB buffer and incubated with 1 µg of 100 bp DNA ladder (New England Biolabs # N3231S) or mononucleosome (Active motif # 81070) for 10 min on ice. After 1,000 rpm spin for 5 min at 4°C, supernatant representing the unbound DNA was loaded on a 6% TBE DNA retardation gel and detected under UV Transilluminator.

ADP-ribosylation and SET8 methyltransferase assays: For ADP-ribosylation assay, PARP1 recombinant enzyme (from 20 to 50 nM per reaction) was incubated with different substrates including either His-SET8 full-length recombinant protein, SET8 peptides or GST, GST-SET8 full-length or mutants and activated using EcoRI hairpin oligo as described above. The reaction was performed in 1x buffer (50 mM Tris.Cl, pH.8, 4 mM MgCl2 and 250 µM DTT) in the presence or absence of cofactor ß-Nicotinamide adenine dinucleotide (0.5 mM NAD+ per reaction, New England Biolabs # B9007S) at RT during 15 min in 20 µl total reaction volume. The reaction was then loaded on 10% Tricine gels and subjected to Western blotting. ADP-ribosylation was detected by mono/poly-ADP-ribose (Cell Signaling Technology # 83732S) or polyADP-ribose (monoclonal 10H, Santa Cruz Biotechnology # sc-56198) antibodies.

For mass spectrometry analyses, 500 nM of PARP1 recombinant enzyme was incubated with 160 µM SET8 peptide (158-170 aa: KKPIKGKQAPRKK and 86-98 aa: KPLAGIYRKREEK) from 1 hr to overnight at RT.

Histone methyltransferase assays were carried out as described previously [41]. SET8 recombinant enzyme (New England Biolabs # M0428S) was incubated with recombinant active PARP1 (Trevigen # 4668-100-01) with or without EcoRI hairpin oligo or NAD+ in histone methyltransferase buffer and 6 µM of radiolabeled [3H] AdoMet (Perkin Elmer Life Science # NET155V001MC). Recombinant human histone H4 (New England Biolabs # M2504S) was used as a substrate. Filter disc method was used to process the samples and the [^{3}H]CH3 incorporated into the H4 protein was determined using a liquid scintillation counter.

LC-MS analysis of poly ADP-ribosylated peptides

Peptide solutions were analyzed with ProxeonII nLC – LTQ Orbitrap XL by direct injection on Reprosil-Pur C18-AQ 3µm 25cm column and eluted at 300nL/min. Full scan MS was acquired FT Resolution 60k in orbitrap MS. The most abundant three ions were selected for data-dependent

CID MS/MS fragmentation with normalized collision energy 26. Using the same nanoLC conditions, HCD MS/MS fragmentation was acquired using quadrupole-orbitrap with NCE 27. Isotope peak intensity areas were determined with SIEVE 2.2.58. (Thermo Fisher Scientific) following chromatographic alignment. Chromatographic extracted ions were plotted with the manufacturer's software XCalibur. Potential location of ADPr unit was screened using a match score modeling of fragment ions in CID MS/MS spectra. The matching score was calculated with Peptide Sequence Fragmentation Modeler, Molecular Weight calculator (https://omics.pnl.gov/software/molecular-weight-calculator). The algorithm is based on Sequest Sp preliminary score but differs in treatment of immonium ions (42). The HCD spectra were mapped manually to the sequence of ADP-ribosylated peptides.

Chromatin immunoprecipitation sequencing (ChIP-seq): HeLa cells overexpressing PARP1 or knockdown PARP1 with esiRNA as mentioned above were subjected to ChIP-seq. Briefly, chromatin was extracted as described above and crosslinked with 1% formaldehyde for 10 min and quenched with 0.125 M glycine. After sonication, H4K20me1 IP was performed overnight in TD buffer as described above using 5 µg of H4K20me1 antibody (Thermo Fisher Scientific # MA5-18067). After antibody capture with protein G magnetic beads and 3 washes with TD buffer, beads were incubated at 65°C overnight in buffer including 50 mM Tris-HCl, pH 7.5, 200 mM NaCl, 1% SDS and 1.6 U/µl of proteinase K (New England Biolabs # P8107S) to reverse crosslinks. DNA from supernatants was extracted using phenol/chloroform procedure. Between 1 and 10 ng of DNA were used to generate DNA libraries for subsequent sequencing analyses. DNA libraries were made using NEBNext Ultra II DNA Library Prep Kit for Illumina (New England Biolabs # E7645S) according to the manufacturer's recommendations.

RNA-sequencing (RNA-seq): RNA from HeLa cells overexpressing PARP1 or knockdown PARP1 with esiRNA as mentioned above was extracted using Quick-RNA Miniprep Kit (Zymo Research # R1054). 1 µg of RNA was used to isolate Poly(A) mRNA using NEBNext Poly(A) mRNA Magnetic Isolation Module (New England Biolabs # E7490S). NEBNext Ultra II directional RNA Library Prep Kit for Illumina (New England Biolabs # E7760S) was used according to the manufacturer's recommendations to generate cDNA and DNA libraries for subsequent DNA sequencing analyses.

NicE-sequencing (NicE-seq): HeLa cells overexpressing PARP1 or knockdown PARP1 with esiRNA as mentioned above were crosslinked with 4% formaldehyde for 10 min at RT. Formaldehyde was quenched using 0.125M of glycine. NicE-seq was performed according to (43) using 5mdCTP in the nucleotide mixture as described in (44).

Data analysis

ChiP-seq data processing: The raw fastq sequences were trimmed using Trim Galore (http://www.bioinformatics.babraham.ac.uk/projects/trim_galore/) to remove the adapters and low-quality sequences. Trimmed reads were mapped to the human reference assembly hg38 using Bowtie2 (45). Aligned reads in bam format were filtered for duplicates and low-quality alignments using Picard (http://broadinstitute.github.io/picard/) and samtools (46). The aligned bam files of technical replicates were merged using Sambamba (47). H4K20me1 enriched regions were identified by calling broad peaks (target over input) using MACS2 (48). Signal tracks were generated using deeptools bamCoverage (49) with the parameters, -normalizeUsing RPKM -of bigwig -e. Pearson correalation analysis was performed using deeptools plotCorrelation (49) function. H4K20me1 peaks were annotated using HOMER (50) annotatePeaks.pl. Repeats elements were annotated using HOMER (50). H4K20me1 profile in the gene regions for PARP1 overexpressed and knockdown HeLa cells and its respective controls was computed with the deeptools computeMatrix and plotProfile (49) functions. Peak length was calculated for all the conditions to estimate the gain and loss of H4K20me1 after PARP1 overexpression and knock down. Transcription factor binding motifs enrichment near H4K20me1peaks was searched using the HOMER tool findMotifsGenome.pl (50) with default parameters. The enrichment scores (-10log(P-value) of individual TF binding motifs were calculated for PARP1 overexpressed and knockdown HeLa cells and their respective controls. Then the enrichment scores were summarized into a data matrix in R (51) and a heatmap was then created to represent condition-specific enrichment of TF binding motifs near the H4K20me1 peaks. ChIP-seq datasets of histone marks H3K36me3 (52), H3K27me3 (52), H3K9me3 (52) and H4K20me3 (16) for HeLa cells were downloaded from human Encyclopedia of DNA Elements (ENCODE) projects and GEO. Genomic regions were visualized using Integrative genomic viewer (IGV) (53).

ChromHMM: ChromHMM (54) was used to create epigenomic segmentations for PARP1 overexpressed and knockdown HeLa cells and their respective controls using bam files for ChIP-seq of H4K20me1, H4K20me3, H3K27me3, H3K9me3, and H3K36me3. Except for H4K20me1, all other ChIP-seq data were downloaded from ENCODE and GEO. A 15-state model was trained using 200 bp bins (LearnModel -b 200) and genome version hg38.

RNA-seq: The raw fastq files were trimmed and quality check was performed using Trim Galore and FASTQC (https://www.bioinformatics.babraham.ac.uk/projects/fastqc/) respectively. All the samples were in good quality. Trimmed reads were mapped to the human reference assembly hg38 using STAR (55). Transcript abundance was estimated from these high-quality mapped reads using htseq count module (56). DESeq2 (57) was used to normalize the count

matrix and identification of differentially expressed genes. Genes that were showing logFC≥0.5 at FDR < 0.05 and logFC≤0.5 at FDR < 0.05 were considered up-regulated genes and down-regulated respectively. Volcano plot, Venn diagram, and heatmaps were generated using R (51).
NicE-seq: NicE-seq data analysis for PARP1 overexpressed and knockdown HeLa cells and their respective controls were done as mentioned in (58).

Results:

PARP1 ribosylates SET8: In a proteomic analysis of SET8 pull-down in HEK293T cells, we discovered that PARP1 is a strong binder (Table S1). To reconfirm this observation, we performed reciprocal immunoprecipitation either with anti-SET8 or anti-PARP1 antibody, and performed western blot, and probed the blots with respective antibodies. Indeed, PARP1 pulled down SET8 and vice-versa, compared to IgG control (Fig. 1A). This led us to investigate if this interaction is cell cycle-dependent, since SET8 expression is cell cycle-dependent (59). For this experiment, we transfected COS-7 cells with FLAG-PARP1 and GFP-SET8 and studied their association using confocal microscopy. The same cells were also probed with an anti-PCNA antibody to examine the chromatin replication foci. Indeed, PCNA remained punctate in the nucleus, so as GFP-SET8, and both were colocalized. However, as expected PARP1 remained throughout the nucleus and appeared as prominent punctate foci with both PCNA and SET8 as observed by bright yellow spots (Fig 1B). These observations suggest that PARP1 has multiple targets throughout the nucleus, but also has strong colocalization with SET8 at the chromatin replication foci. To narrow down the exact binding motifs between PARP1 and SET8, we performed a reciprocal GST-pulldown assay. Immobilized GST fusion of overlapping SET8 fragments covering the entire protein was challenged with full-length PARP1. After stringent washes, the bound proteins were denatured in SDS gel loading buffer and separated on SDS-PAGE followed by blotting onto a membrane for western blot with anti-PARP1 antibody to determine the binding domain. Two fragments covering both N-terminal 1-98 amino acids and disorder domain 80-230 amino acids residues showed binding. Although, a stronger binding was observed with the disorder domain (DD) (Fig 1C, left panel; Fig. S1A). SET8 disordered domain is unfolded and has charged amino acids residues such as lysines that may aid in binding (Fig. S1B). To investigate the binding amino acids, GST-SET8 fusion was mutated at K86A, K158/159A, K162/164A, R168A, K169/170A, K174A and full-length purified GST fusion SET8 mutant (GST-SET8FLmut) was challenged with PARP1. We observed significant (~70%) loss of binding by PARP1, confirming PARP1 binding occurs on SET8 DD (Fig. S1C). A similar reciprocal GST pulldown experiment using immobilized GST-PARP1 fusion fragments covering the entire protein was challenged with full-length SET8. The bound proteins were western blotted and probed for SET8 to reveal GST-PARP1 DNA binding domain (GST-PARP1DB) as the strongest binder (Fig 1C, right panel). Based on the results of both the colocalization and GST pulldown experiments, we concluded that both SET8 and PARP1 are indeed binding partners.

We next investigated the functional consequence of this interaction. Both purified SET8 and PARP1 were incubated together in the absence or presence of cofactor NAD+ for various lengths of time, between 2-15 min. The reactions were stopped, and the proteins were separated on SDS PAGE and western blotted with anti-PAR (anti-poly ADP ribose) antibody. If the proteins are ribosylated, an anti-PAR antibody will show higher molecular weight for the

proteins. We observed auto-poly-ADP-ribosylation of PARP1 as expected only in the presence of NAD+ (Fig 1D, upper panel; Fig. S2A). We also observed a strong reaction time-dependent SET8 poly ADP-ribosylation. Indeed, all SET8 molecules were poly ADP-ribosylated by PARP1 as observed by high molecular weight migrating smear (Fig 1D). We further investigated poly ADP-ribosylated regions of SET8 by performing *in vitro* poly ADP-ribosylation assay of overlapping peptides, western blotting and probing the blot with anti-PAR antibody. We found that GST-SET8 DD is indeed the substrate of PARP1 (Fig. S2B). We narrowed down the amino acid residues 81-98 and 157-180 as the putative acceptor of ADP-ribose for poly ADP-ribosylation (Fig. S2C, D).

LC-MS analysis of PARP1 activity on SET8 peptides: To determine the nature of poly-ADP-ribosylation and the acceptor amino acid, we made synthetic peptides covering 86-98 and 158-170 amino acids and performed *in vitro* poly ADP-ribosylation and analyzed the reaction product using LC-MS. First, we monitored the PARP1 activity with SET8 peptide KPLAGIYRKREEK-NH2 (86-98 aa). Peptides with an amidated C-terminus require specific conditions for detection to support MS/MS sequencing identification (60). We detected and quantified signals for the three main isotopes starting with 0 min (negative control) and incubation with PARP1 for 1hr, 4hrs and overnight (Fig. S3A). We observed a decrease in the signal of the KPLAGIYRKREEK-NH2 peptide after the initial 1hr incubation. Concomitantly, we assessed the peak areas for two charged states (+3, +4) of the (ADPr) KPLAGIYRKREEK-NH2 in order to detect the activity of PARP1 (Fig. S3B, C). Three main isotopes for each charge state showed the signal of (ADPr)KPLAGIYRKREEK-NH2 present at 1hr followed by a decrease in intensity at 4hrs and overnight reactions. This suggested the formation of additional species beyond the initial addition of one ADP-ribosylation unit. Next, we investigated the peptide signals at two faster PARP1 reaction times, 5 min and 15 min. Chromatographic ion signals for (1ADPr)KPLAGIYRKREEK-NH2 were detected for both charge states +3 and +4 at retention time 8.35 min (Fig. S3D). The minimal chromatographic signal was detected for (2ADPr)KPLAGIYRKREEK-NH2 with an increased elution time of 10.33 min. At 15 min reaction time, the signal for di-ADP-ribosylated peptide near 10.3 min increased with a wider base (Fig. S3E). A second peak with intermediate hydrophobicity relative to the mono ADP-ribosylated peptide showed the most intense di-ADP-ribosylation signal at RT 9.77 min (Fig. S3E). Therefore, we detected the formation of possible diastereomers of increased hydrophobicity upon addition of 1ADPr unit to mono ADP-ribosylated peptides during a 10 min reaction time interval.

Characterization of MS/MS HCD fragmentation pattern of (ADPr) KPLAGIYRKREEK-NH2 peptide is presented in figure S4. For charge state +3, we observed the formation of fragment ions m3, m5, and m8 that are independent of the peptide sequence and indicative of the ADP-ribose

group (Fig. S4A, top panel). The nomenclature for ADP ribosylation fragment ions is according to Hengel et al. (61). Similarly, but with lower intensity, charge state +4 showed confirmed the presence of these fragment ions m3, m5 and m8 (Fig. S4B, top panel). Intact peptide backbone ions containing partial ADP ribose group and peptide y sequencing ions can be visualized at m/z 500 – 900 (Fig. S4A, B, bottom panels; Fig. S4B is the same spectrum from Fig 1E). In addition to HCD spectra, CID spectra can be probed for ADP-ribosylation information of amidated C-terminus peptides. We screened seven amino acids for the position of the ADPr unit (Fig. S5). For both charges +3 and +4, the associated MS/MS spectra mapped with a higher score the N-terminal lysine of KPLAGIYRKREEK-NH2.

Analysis of SET8 peptide KKPIKGKQAPRKK-NH2 (158-170 aa) showed that activity of PARP1 resulted in maximum signal for 1ADPr unit addition at charge +4 for overnight reaction (Suppl Fig 6B). Detection of lower intensity peak areas for all three main isotopes of charge +4 together with moderate signal decrease of unmodified KKPIKGKQAPRKK-NH2 (Fig. S6A) suggested a slower PARP1 kinetic towards this SET8 peptide. For comparison, CID MS/MS spectrum of this charge state with unit resolution linear ion trap showed the presence of ADP-ribose signature ions (Fig. S7). Taken together, we found multiple K residues were poly ADP-ribosylated, including K86, K153, K162, and K164 (Fig 1E).

PARP1 poly ADP-ribosylates SET8 impacting DNA, nucleosome binding and catalytic activity: SET8 is well known for its interaction with nuclear proteins, PCNA, a processivity factor involved in DNA replication and required for S-phase progression (59,62). A crystallography study demonstrated that SET8 employs its i-SET and c-SET domains to engage nucleosomal DNA 1 to 1.5 turns from the nucleosomal dyad (63). To evaluate the DNA binding activity of SET8, we incubated a 100 bp DNA ladder with various GST-fusion fragments of SET8, GST-SET8 full-length and GST-SET8 full-length catalytic mutant. After the incubation time, we resolved fusion proteins -DNA or nucleosome complexes on the gel. If a defined size of DNA gets complexed with protein, that DNA band will be shifted and will not be represented on the gel compared to the control ladder. As predicted by crystallography, GST-SET8 full-length protein bound predominately to double-stranded DNA ranging between 100-300 bp in the gel-shift assay. This binding was partially dependent on the 157-352 amino acids of SET8, and a significant loss of binding was observed in a deletion mutant comprising 175-352 amino acids, suggesting 157-175 amino acids play a functional role in DNA binding (Fig 2A). We also performed gel shift assay of purified SET8 protein with a fluorescent-labeled double stranded DNA oligo and measured the Kd values of 1.6+/-0.6 µM (Fig 2B). After observing the robust DNA binding activity of SET8, we also validated its binding activity with recombinant mono-nucleosomes using similar GST-SET8 fusions that were used for DNA binding activity studies shown in figure 2A. Once again, 157-175 amino acids played a functional role in nucleosome binding (Fig 2C).

Taken together, data from previous crystallography studies and our gel-shift assays, we conclusively demonstrated that SET8 has both double-stranded DNA and nucleosome binding activity.

Since SET8 is a substrate for PARP1, we investigated the role of DNA in SET8-PARP1 binary complex formation, and if poly ADP-ribosylation can affect either DNA or nucleosome binding activity of SET8. Since DNA is a catalytic activator of PARP1, we incubated GST-SET8, DNA and PARP1 in the presence and absence of DNase I and performed GST-pull down assay followed by western blotting and probing the bound proteins with respective antibodies. Indeed, both GST-SET8 and PARP1 formed binary complexes in the presence of double-stranded DNA. However, in the presence of DNase I, SET8-PARP1 binding was reduced confirming DNA as a facilitator of binary complex formation (Fig. S8A, B).

Subsequently, we incubated SET8 with either a 100 bp ladder or with a recombinant mononucleosome in the presence of PARP1 and NAD+ for poly ADP-ribosylation, and the control remained without NAD+ cofactor. Indeed, poly ADP-ribosylated SET8 lost the DNA as well as nucleosome binding activity as observed by prominent DNA or nucleosome bands (Fig 2D, top panel). To confirm that this observation is due to poly ADP-ribosylation, a portion of the same reaction was western blotted and probed with anti-PAR antibody. Indeed, the SET8 poly ADP- ribosylation was evident in those lanes that had poor binding of DNA or nucleosome with GST-SET8 (Fig 2D middle panel). We hypothesized that the loss of binding activity of SET8 on DNA and/or nucleosome would impact its catalytic activity on chromatin. To evaluate if SET8 methyltransferase activity on histone H4 is modulated by PARP1 mediated poly ADP-ribosylation, we performed *in vitro* histone methyltransferase assays mimicking either poly ADP-ribosylated SET8 or its native form. To initiate poly ADP-ribosylation of SET8, we pre-incubated SET8, PARP1, DNA and NAD+ for 15 min at room temperature, followed by the addition of methyl donor, tritiated AdoMet, and purified recombinant histone H4 to initiate H4K20 monomethylation. After the reaction, we performed the filter binding assay for tritium incorporation on substrate histone H4 was measured. Indeed, poly ADP-ribosylation SET8 lost ~40-50% activity compared to the control that lacked any one component for successful poly ADP-ribosylation (Fig 2E). These results suggest that PARP1 not only inhibits SET8 binding to DNA and nucleosome, but it can also impact histone H4K20 monomethylation.

Poly ADP-ribosylation promotes SET8 degradation and facilitates H4K20me3: Poly ADP-ribosylation was recently identified as a signal for triggering protein degradation through the ubiquitin-proteasome system. Indeed, poly ADP-ribosylation-mediated degradation of ARTD1 (ADP-ribosyltransferase diphtheria toxin-like 1) is documented (64). In another example, PARP1 binds and poly ADP-ribosylates bromodomain-containing protein 7 (BRD7), which enhances its

ubiquitination and degradation through the PAR-binding E3 ubiquitin ligase RNF146 (65). This led us to investigate if PARP1 has any modulating effect on SET8 levels in the cell. First, we transfected cells with either FLAG or FLAG-PARP1 construct and measured the transfection efficiency by western blotting and probing with anti-FLAG antibody, followed by probing the blot with anti H4K20me1, 2 and 3 along with SET8 and Suv420H1. Indeed, PARP1 overexpression had reduced SET8 and its reaction products, H4K20me1 to almost half of the control (Fig. S9A, B). We then systematically transfected HA-ubiquitin with GFP-SET8 or FLAG-PARP1 alone or co-transfected all three constructs into the mammalian cells and treated the cells with proteasome inhibitor MG132. We performed western blots of cell extracts to evaluate transfection efficiency and expression of constructs. Probing the blot with anti-GFP antibody demonstrated equivalent expression GFP-SET8 fusion in all transfected samples. Similarly, anti-FLAG antibody probing of the blot showed robust expression of FLAG-PARP1 fusion protein (Fig 3A, upper panel). Next, we immunoprecipitated GFP-SET8 fusion with anti-GFP antibody and probed the western blot with anti-HA to detect HA-ubiquitinated SET8 fusion or anti-PAR for poly ADP-ribosylated SET8 fusions. Indeed, GFP-SET8 showed high molecular weight HA-ubiquitinated smear when expressed alone with HA-ubiquitin (Fig 3A, lower panel, lane 1). GFP-SET8 co-expression with FLAG-PARP1 and HA-ubiquitin resulted in accumulation of high molecular weight HA-ubiquitinated smear, suggesting that the expression of additional PARP1 enhances ubiquitination of GFP-SET8 (Fig 3A, lower panel, lane 2). Similarly, blocking ubiquitination of GFP-SET8 by MG132 resulted in higher amounts of high molecular weight HA-ubiquitinated smear as expected. When we co-expressed GST-SET8, FLAG-PARP1 and HA-ubiquitin and blocked protein degradation using MG132, we observed ~ 5 folds accumulation of HA-ubiquitinated GST-SET8 protein (Fig 3A, lower panel, lane 4). Similarly, ribosylated GFP-SET8 was more prominent in GFP-SET8 and FLAG-PARP1 overexpressed cells (Fig 3A, lower right panel, lane 2 and 4). All these experiments conclusively prove that PARP1 is an effector protein that aids in poly ADP-ribosylation of SET8 leading to ubiquitin-mediated degradation.

The SET8 is ubiquitinated on chromatin by CRL4(Cdt2) complexes during S phase and following DNA damage in a PCNA-dependent manner. In a transgenic mouse model for lung cancer, the level of SET8 was reduced in the preneoplastic and adenocarcinomous lesions following over-expression of Cul4A (66). Therefore, it is expected that down regulation of Cul4A by siRNA would lead to accumulation of SET8. Similarly, downregulation of PARG, that removes ADP ribose from poly ADP-ribosylated protein by PARP1 and acts as an antagonist of PARP1, would also lead to the accumulation of SET8. To validate our hypothesis, we transfected GFP-SET8 fusion constructs to mammalian cells and treated the cells with DMSO, Cul4A inhibitor (MLN4924), or PARG inhibitor (PDD00017273) and monitored the SET8 pattern of expression by immunoprecipitation and western blotting. Indeed, GFP-SET8 fusion protein was expressed in a similar level in the absence or presence of either Cul4A or PARG inhibitor. Immunoprecipitation

of GFP-SET8 showed more prominent high molecular weight poly ADP-ribosylated GFP-SET8 fusion in PARGi treated cells (Fig. 3B). Taken together with results from figure 3A and B, we correlate that high molecular weight ubiquitinylated GFP-SET8 are both ubiquitinylated and poly ADP-ribosylated, suggesting a cross-communication between both to maintain a steady-state level of SET8 in the cells.

We next knocked down PARP1 using siRNA to define its role in SET8 stability conclusively. HeLa cells were treated with control siGFP, siPARP1 and siSET8 and the extracts were western blotted and probed with respective antibodies. As expected, anti-PARP1 was able to knock down 70% PARP1 resulting in 1.5-fold increase in SET8 level. Surprisingly, SET8 level increase did not translate into an increase in H4K20me1 level (Fig 3C). This led us to investigate global H4K20me2/3 heterochromatic marks in the knockdown cells using western blot. Surprisingly, H4K20me2 level decreased along with the concurrent gain of H4K20me3 suggesting knockdown of PARP1 facilitates the rapid formation of H4K20me3 that may result in aberrant heterochromatic mark establishment.

Cell cycle dependent interaction of SET8 and PARP1: Since overexpression of PARP1 led to SET8 degradation and both SET8 and H4K20me1 are crucial to cell cycle progression genome stability, DNA replication, mitosis, and transcription, we hypothesized that SET8 and PARP1 would be colocalized in cells in a cell cycle-dependent manner. Thymidine-nocodazole treated synchronized HeLa cell nuclei were isolated and extracts were made corresponding to G1, S and G2M phase. Equal amounts of extracts were evaluated for the relative abundance of SET8, PARP1, and H4K20me1 using western blot with respective antibodies. CDT1 (G1 phase marker) was used as a positive control for cell cycle synchronization. As expected, SET8 level was lowest during S phase and highest at G2/M phase, mirroring H4K20me1 levels. PARP1 level remained unchanged throughout the cell cycle (Fig. 4A). Since SET8 and PARP1 directly interact, we hypothesized this interaction might affect SET8 levels on the chromatin. To validate this hypothesis, we used G1, S, G2/M nuclear extracts for SET8 immunoprecipitation (IP). The captured proteins were resolved on SDS-PAGE, western blotted and probed with SET8 and PARP1 antibodies (Fig 4B). We observed the highest amounts of SET8 being captured in G2/M compared to S or G1 phase. SET8 IP also revealed that PARP1 is co-immunoprecipitated in G2/M compared to G1 or S phase. However, all three phases with PARP1 co-immunoprecipitated with SET8, abate a higher amount during S phase. We, therefore, quantified relative coimmunoprecipitation between PARP1-SET8 during all three cell cycle phases by comparing the ratios between PARP1 and SET8 in 3 independent experiments (Fig 4B, bottom panel). Indeed, PARP1/SET8 ratio was highest during S phase compared to the lowest in G2/M, confirming PARP1 indeed modulates SET8 stability on the chromatin in a cell cycle-dependent manner that is reflected by both enzyme level and H4K20me1.

In another experiment, we pulse changed COS-7 cells with 5-ethynyl-2'-deoxyuridine (EdU) to selectively labeled the newly synthesized DNA in S phase, for rapid visualization and its ability not to interfere with subsequent antibody staining. The same cells were also transfected with GFP-SET8 and further probed with anti-PAR antibody. EdU formed the punctate pink nuclear staining pattern, typical of S phase. And the same regions were also visualized as yellow indicating GFP-SET8 colocalization. Poly ADP-ribosylation was visualized using anti-PAR antibody as red throughout the nucleus, as expected with clear colocalization at the replication forks and SET8 (Fig 4C). These results confirm poly ADP-ribosylation of SET8 occurs at the S phase as observed by IP (Fig 4B).

PARP1 level regulates H4K20me1 domain in genome: Since PARP1 level increases at S phase with a concurrent decrease in SET8 and H4K20me1 level, we next investigated if there is a functional implication of PARP1 level in the cell and H4K20me1 distribution on the chromatin. For this investigation, we either knockdown or overexpressed PARP1 in HeLa cells and performed H4K20me1 ChIP-seq with respective controls. Prior to the ChIP-seq, we western blotted the samples and observed similar levels of SET8 and H4K20me1, me2 and me3 as observed for PARP1 knockdown or overexpression (Fig. 3C and Fig. S9). Since both experiments required different transfection reagents, the control and experimental datasets were compared separately. The Pearson's correlation between the ChIP-seq fragments between control FLAG vs. overexpressed FLAG-PARP was 0.97. Similarly, siGFP and siPARP knockdown correlation values were 0.98 (Fig. S10A, B). This suggests the tag density between the overexpression and knockdown has similar H4K20me1 reads. Furthermore, we extracted H4K20me1 ChIP-seq data and mapped it on TSS and TTS flanking -2kb upstream and +2 kb downstream. The metagene plot of genes didn't show any significant changes of H4K20me1 in PARP1 overexpressed cells, although the regional density of H4K20me1 displayed variation. However, the knockdown of PARP1 indeed hypermethylated H4K20me1 in both gene body as well as 2.0 kb up- and down-stream of both TSS and TTS (Fig. 5A, B).

The concurrent gain of H4K20me1 regional density in the intron and loss in the intergenic regions when PARP1 is knockdown or overexpressed, suggest any alterations in PARP1 levels impacts the aberrant distribution of H4K20me1 marks in cells (Fig. S10C). These regions are rich in LINE and SINE elements that function to regulate gene expression by affecting chromatin structure and gene transcription. We extracted the regional distribution of H4K20me1 in LINE and SINE from ChIP-seq datasets and observed that PARP1 knockdown enriched H4K20me1 on the LINE elements and decreased the mark on SINE elements, and the reverse was true in PARP1 overexpressed cells (Fig. S10D). Subsequently, we compared H4K20me1 distribution in the genic regions consisting of 57623 genes representing the entire hg38 reference, in both

PARP1 overexpression or knockdown and compared to respective chromatin accessibility and RNA expression features. As expected, H4K20me1 distribution and chromatin accessibility tag densities were highly correlated with a Pearson's coefficient of 0.97, confirming H4K20me1 distribution and chromatin accessibility as an interdependent phenomenon as reported previously (Fig. 5C, 18). In a parallel comparison between knockdown set and their chromatin accessibility also yielded a high Pearson's coefficient of 0.94 (Fig. 5D). A similar correlation between H4K20me1 profile between knockdown or overexpression with their respective RNA expression profile, yielded similar Pearson's coefficient value of 0.64-0.67 (Fig. 5E, F). In addition, chromatin accessible profile of the genes essentially remained similar in either the PARP1 overexpression or depletion as observed in metagene plots (Fig. S11A, B). Taken together we concluded that neither overexpression of PARP1 or depletion of PARP1 had any significant difference of H4K20me1 in accessible regions, as well as in mRNA expressions.

Since H4K20me1 directly facilitates chromatin accessibility and promotes transcription of housekeeping genes (18), we extracted H4K20me1 ChIP-seq positive genes from RNA-seq data in PARP1 overexpression and knockdowns and compared them with respective controls. We hypothesized that PARP1 overexpression or knockdown would result in redistribution of H4K20me1 marks in the genome. Comparison between cells transfected with control FLAG and FLAG-PARP1 as well as control siGFP and siPARP1 displayed both loss and gain of H4K20me1 mark in expressed genes. In the overexpression of FLAG and FLAG-PARP1, 5 H4K20me1 mark genes were lost and 1 was gained in PARP1 overexpression. Similarly, in PARP1 knockdown, 21 genes lost the H4K20me1 mark compared to 24 that gained the mark (Fig. S11C, D). We further compared H4K20me1 peak width in the above set of experiments. In PARP1 overexpression, we observed gain of 200-500 bp and loss in 1-2.5 kbp H4K20me1 regions. Similarly, in PARP1 knockdown loss in 200-500 bp and gain in 2.5-10 kbp H4K20me1 regions, confirming the aberrant distribution of H4K20me1 in the genome resulting in alteration of peak width (Fig. 5G). We further examined if the aberrant deposition of H4K20me1 has any influence on RNA expression. Comparison between H4K20me1 peak width and RNA expression tag densities presented four different scenarios. (1) In response to PARP1 overexpression the H4K20me1 peak width decreased resulting in either higher RNA expression, exemplified in FSH gene. (2) Or lower RNA expression, exemplified in AXIN2 gene. (3) In response to PARP1 depletion the H4K20me1 peak width increased resulting in either higher RNA expression, exemplified in KLF2 gene. (2) Or lower RNA expression, exemplified in FOXC2 gene (Fig. 5H, I). These results clearly demonstrate that alteration in SET8 enzyme level either by PARP1 overexpression or knockdown can lead to aberrant H4K20me1 in the genome, effectively influencing its territorial boundaries and affecting gene expression without altering the chromatin state (Fig. S11E). The genes differentially expressed by PARP1 overexpression or knockdown are listed in Table S2A and B.

Enrichment of consensus TF-binding motifs near H4K20me1: Further analysis of the sequence tags obtained from H4K20me1 ChIP-seq and the consensus transcription factor binding sites analysis shows that PARP1 overexpression or knockdown in cells leads to enrichment or decrease of some transcription factor (TF) binding sites in its vicinity. Most of those TF binding site enrichment are associated with the Wnt/beta-catenin pathway (Fig. S12A, B). For example, TCF3, a transcriptional repressor implicated in the Wnt pathway by directly binding to beta-catenin was observed to be PARP1 regulated. The PARP1 dependent TF enrichment sequences with H4K20me1 chromatin signature fell into four general categories. (1) Overall PARP1 level regulated TF binding site enrichment, described as present in control cells, but not when overexpressed, including Bapx1, CHR, STAT5, MYB, Tcf7, etc. (2) PARP1 induced TF binding site enrichment, described as enriched in cells where PARP1 is overexpressed, including DMRT1, Stat6, TEAD4, etc (Fig. S12A). (3) PARP1 dependent TF binding site enrichment, described as reduction in cells when PARP1 is depleted, including Nur77, GATA5, YY2, VDR, CHR, etc. (4) PARP1 inhibited TF binding site enrichment, described as enriched in cells when PARP1 is depleted, including Foxa2, Elk1, Pbx1, SPIC, etc (Fig. S12B). Therefore, it is plausible that PARP1 mediated mis-regulation of H4K20me1 domains are linked to gene expression via transcription factor recruitment. Indeed, the TF binding motif analysis displayed ~80% of the Wnt signaling pathway associated TFs were differentially enriched due to PARP1 overexpression and a slightly high level, ~70% were enriched in PARP1 knock down cells (Table S3A and B). These observations suggest that optimal PARP1 level is essential for TF motif enrichment that could affect gene expression and cellular development.

Discussion:

The principal enzyme of poly ADP-ribosylation is PARP1. While many studies have reported that PARP1 promotes gene transcription, it also promotes gene expression at the post-transcriptional level by modulating the RNA-binding protein HuR (67,68). Indeed, PARP-1 is required for a series of molecular outcomes at the promoters of PARP-1 regulated genes, leading to a permissive chromatin environment for RNA Pol II machinery loading. Poly ADP-ribosylation has an important role in the maintenance of H3K4me3, as the enzyme for demethylation, KDM5B, is impaired by poly ADP-ribosylation. Consistently, an increased level of KDM5B at TSS of active genes is associated with decreased H3K4me3 after inhibition of poly ADP-ribosylation *in vivo*. (69). There is also *in vitro* evidence of a direct involvement of poly ADP-ribosylation in the crosstalk between H3 and H1 methylation. Indeed, poly ADP-ribosylation of H3 impairs its methylation by the H3K4 mono-methyltransferase SET7/9, thus shifting its catalytic activity towards other lysine residues of H1 (70). Another role of poly ADP-ribosylation can contribute to transcriptional repression by H3K9me2 accumulation at retinoic acid (RA)-dependent genes. In this mechanism, demethylase KDM4D is covalently poly ADP-ribosylation at the N-term domain, impairing its recruitment onto RA-responsive promoters, leading to repression by H3K9me2 accumulation (71). Apart from the transcriptional role of PARP, inhibition/depletion of the enzymes also causes loss of epigenetic marker on heterochromatin, H3K9me3 (72), H4K20me3 (73), and 5mC (74) at the centromeric regions. These all studies suggest that PARP enzymes can modulate chromatin structure and regulate gene expression.

In this study, poly ADP-ribosylation not only impaired SET8 catalytic activity, it also ribosylated and facilitate SET8 degradation by the ubiquitin pathway. As expected, knockdown of PARP1 resulted in accumulation of SET8 in cells, although it did not increase H4K20me1 load on chromatin. However, there was a profound decrease of H4K20me2 and corresponding increase in H4K20me3. This is not unexpected since H4K20me2 is the precursor of heterochromatin mark H4K20me3. This was further supported by the FLAG-PARP1 overexpression studies. Indeed, overexpression of PARP1 not only decreased the level of SET8, it also correspondingly decreased the level of H4K20me1, H4K20me2 and H4K20me3. Taken together, these results suggest an alteration in the level of SET8 in cells can profoundly impact heterochromatic mark H4K20me3. An increase in H4K20me2/3 may have resulted in heterochromatic domain rearrangement in overexpressing cells. However, previous studies have reported poly ADP-ribosylated PARP1 might conflict with CG methylation by non-covalent interaction with DNMT1 preventing its access on DNA and catalysis (74). PARP1 also affects DNA methylation by forming a complex with the transcription factor CTCF. In another report, PARP1 was shown to control the UHRF1-mediated ubiquitination of DNMT1 to timely regulate its abundance during S and G2 phase, thus impacting CG methylation. Therefore, the above observations, and our current

studies, demonstrate other epigenetic marks particularly DNA methylation and SET8 levels in the cell, may play a role in chromatin H4K20me1 domain maintenance. SET8 is known to regulate chromatin compaction during G1 phase (18). Therefore, it would make sense that during this phase there is little interaction between PARP1 and SET8. Indeed, upon mitotic exit, chromatin relaxation is controlled by SET8-dependent methylation of histone H4K20. In the absence of either SET8 or H4K20me1 mark, substantial genome-wide chromatin decompaction occurs allowing excessive loading of the origin recognition complex (ORC) in the daughter cells (18). Based on the results, it is plausible that PARP1 overexpression in cancer would catalytically compromise SET8 leading to reduced H4K20me1. This would have a larger ramification in H4K20me3 level on heterochromatin. Since H4K20me3 represses transcription when present at promoters and silences repetitive DNA and transposons, its aberrant deposition on chromatin may alter the transcriptional network during oncogenesis. Furthermore, SET8 mediated H4K20me1 regulates Pol II promoter-proximal pausing by regulating H4K16ac and H4K20me3 levels and ultimately transcriptional output (75). Therefore, PARP1 mediated poly ADP-ribosylation can impact epigenome inheritance, structure, and gene expression.

Data availability

ChIP-seq, RNA seq and NicE-seq data performed in this study are available in NCBI Gene Expression Omnibus (GEO) under the accession GSE188744.

Acknowledgments: We thank W. Jack and C. Carlow for critical reading of the manuscript, T. Evans, D. Comb, Sir R.J. Roberts and J. Ellard for encouragement.

Competing interests: The authors declare that they have no competing interests

Funding: The project was funded by basic research grant to SP from the New England Biolabs, Inc.

Author contribution: POE, CR, HGC performed experiments. VUS performed data analysis. SP conceptualized the project and wrote the manuscript in collaboration with POE, CR, HGC and VUS.

References:

1. Ma,Y., Kanakousaki,K. and Buttitta,L. (2015) How the cell cycle impacts chromatin architecture and influences cell fate. *Front. Genet.*, 10.3389/fgene.2015.00019.
2. Ho,L. and Crabtree,G.R. (2010) Chromatin remodelling during development. *Nature*, 10.1038/nature08911.
3. Perino,M. and Veenstra,G.J.C. (2016) Chromatin Control of Developmental Dynamics and Plasticity. *Dev. Cell*, 10.1016/j.devcel.2016.08.004.
4. Beagrie,R.A. and Pombo,A.N.A. (2017) Continuous chromatin changes. *Nature*.
5. Ma,Y. and Buttitta,L. (2017) Chromatin organization changes during the establishment and maintenance of the postmitotic state. *Epigenetics and Chromatin*, 10.1186/s13072-017-0159-8.
6. Bannister,A.J. and Kouzarides,T. (2011) Regulation of chromatin by histone modifications. *Cell Res.*, 10.1038/cr.2011.22.
7. Lieberman-Aiden,E., Van Berkum,N.L., Williams,L., Imakaev,M., Ragoczy,T., Telling,A., Amit,I., Lajoie,B.R., Sabo,P.J., Dorschner,M.O., *et al.* (2009) Comprehensive mapping of long-range interactions reveals folding principles of the human genome. *Science (80-.).*, 10.1126/science.1181369.
8. Kuo,M.H. and Allis,C.D. (1998) Roles of histone acetyltransferases and deacetylases in gene regulation. *BioEssays*, 10.1002/(SICI)1521-1878(199808)20:8<615::AID-BIES4>3.0.CO;2-H.
9. Grunstein,M. (1997) Histone acetylation in chromatin structure and transcription. *Nature*, 10.1038/38664.
10. Smith,B.C. and Denu,J.M. (2009) Chemical mechanisms of histone lysine and arginine modifications. *Biochim. Biophys. Acta - Gene Regul. Mech.*, 10.1016/j.bbagrm.2008.06.005.
11. Herz,H.M., Garruss,A. and Shilatifard,A. (2013) SET for life: Biochemical activities and biological functions of SET domain-containing proteins. *Trends Biochem. Sci.*, 10.1016/j.tibs.2013.09.004.
12. Oda,H., Okamoto,I., Murphy,N., Chu,J., Price,S.M., Shen,M.M., Torres-Padilla,M.E., Heard,E. and Reinberg,D. (2009) Monomethylation of Histone H4-Lysine 20 Is Involved in Chromosome Structure and Stability and Is Essential for Mouse Development. *Mol. Cell. Biol.*, 10.1128/mcb.01768-08.
13. Couture,J.F., Collazo,E., Brunzelle,J.S. and Trievel,R.C. (2005) Structural and functional analysis of SET8, a histone H4 Lys-20 methyltransferase. *Genes Dev.*, 10.1101/gad.1318405.
14. Schotta,G., Sengupta,R., Kubicek,S., Malin,S., Kauer,M., Callén,E., Celeste,A., Pagani,M., Opravil,S., De La Rosa-Velazquez,I.A., *et al.* (2008) A chromatin-wide transition to H4K20

monomethylation impairs genome integrity and programmed DNA rearrangements in the mouse. *Genes Dev.*, 10.1101/gad.476008.

15. Kleine-Kohlbrecher,D., Christensen,J., Vandamme,J., Abarrategui,I., Bak,M., Tommerup,N., Shi,X., Gozani,O., Rappsilber,J., Salcini,A.E., *et al.* (2010) A Functional Link between the Histone Demethylase PHF8 and the Transcription Factor ZNF711 in X-Linked Mental Retardation. *Mol. Cell*, 10.1016/j.molcel.2010.03.002.
16. Cao,X., Chen,Y., Wu,B., Wang,X., Xue,H., Yu,L., Li,J., Wang,Y., Wang,W., Xu,Q., *et al.* (2020) Histone H4K20 Demethylation by Two hHR23 Proteins. *Cell Rep.*, 10.1016/j.celrep.2020.03.001.
17. Karachentsev,D., Sarma,K., Reinberg,D. and Steward,R. (2005) PR-Set7-dependent methylation of histone H4 Lys 20 functions in repression of gene expression and is essential for mitosis. *Genes Dev.*, 10.1101/gad.1263005.
18. Shoaib,M., Walter,D., Gillespie,P.J., Izard,F., Fahrenkrog,B., Lleres,D., Lerdrup,M., Johansen,J.V., Hansen,K., Julien,E., *et al.* (2018) Histone H4K20 methylation mediated chromatin compaction threshold ensures genome integrity by limiting DNA replication licensing. *Nat. Commun.*, 10.1038/s41467-018-06066-8.
19. Abbas,T., Shibata,E., Park,J., Jha,S., Karnani,N. and Dutta,A. (2010) CRL4Cdt2 regulates cell proliferation and histone gene expression by targeting PR-Set7/Set8 for degradation. *Mol. Cell*, 10.1016/j.molcel.2010.09.014.
20. Centore,R.C., Havens,C.G., Manning,A.L., Li,J.M., Flynn,R.L., Tse,A., Jin,J., Dyson,N.J., Walter,J.C. and Zou,L. (2010) CRL4Cdt2-mediated destruction of the histone methyltransferase Set8 prevents premature chromatin compaction in S phase. *Mol. Cell*, 10.1016/j.molcel.2010.09.015.
21. Oda,H., Hübner,M.R., Beck,D.B., Vermeulen,M., Hurwitz,J., Spector,D.L. and Reinberg,D. (2010) Regulation of the Histone H4 Monomethylase PR-Set7 by CRL4Cdt2-Mediated PCNA-Dependent Degradation during DNA Damage. *Mol. Cell*, 10.1016/j.molcel.2010.10.011.
22. Yin,L., Yu,V.C., Zhu,G. and Chang,D.C. (2008) SET8 plays a role in controlling G1/S transition by blocking lysine acetylation in histone through binding to H4 N-terminal tail. *Cell Cycle*, 10.4161/cc.7.10.5867.
23. Frescas,D. and Pagano,M. (2008) Deregulated proteolysis by the F-box proteins SKP2 and β-TrCP: Tipping the scales of cancer. *Nat. Rev. Cancer*, 10.1038/nrc2396.
24. Dephoure,N., Zhou,C., Villén,J., Beausoleil,S.A., Bakalarski,C.E., Elledge,S.J. and Gygi,S.P. (2008) A quantitative atlas of mitotic phosphorylation. *Proc. Natl. Acad. Sci. U. S. A.*, 10.1073/pnas.0805139105.
25. Huttlin,E.L., Jedrychowski,M.P., Elias,J.E., Goswami,T., Rad,R., Beausoleil,S.A., Villén,J., Haas,W., Sowa,M.E. and Gygi,S.P. (2010) A tissue-specific atlas of mouse protein phosphorylation and expression. *Cell*, 10.1016/j.cell.2010.12.001.

26. Olsen,J. V, Vermeulen,M., Santamaria,A., Kumar,C., Miller,M.L., Jensen,L.J., Gnad,F., Cox,J., Jensen,T.S., Nigg,E.A., *et al.* (2010) Quantitative Phosphoproteomics Reveals Widespread Full Phosphorylation Site Occupancy During Mitosis -- Olsen et al. 3 (104): ra3 -- Science Signaling (Supplemental). *Sci. Signal.*
27. Wu,S., Wang,W., Kong,X., Congdon,L.M., Yokomori,K., Kirschner,M.W. and Rice,J.C. (2010) Dynamic regulation of the PR-Set7 histone methyltransferase is required for normal cell cycle progression. *Genes Dev.*, 10.1101/gad.1984210.
28. Alemasova,E.E. and Lavrik,O.I. (2019) Poly(ADP-ribosyl)ation by PARP1: Reaction mechanism and regulatory proteins. *Nucleic Acids Res.*, 10.1093/nar/gkz120.
29. Altmeyer,M., Messner,S., Hassa,P.O., Fey,M. and Hottiger,M.O. (2009) Molecular mechanism of poly(ADP-ribosyl)ation by PARP1 and identification of lysine residues as ADP-ribose acceptor sites. *Nucleic Acids Res.*, 10.1093/nar/gkp229.
30. Teloni,F. and Altmeyer,M. (2016) Survey and summary readers of poly(ADP-ribose): Designed to be fit for purpose. *Nucleic Acids Res.*, 10.1093/nar/gkv1383.
31. Daniels,C.M., Ong,S.E. and Leung,A.K.L. (2015) The Promise of Proteomics for the Study of ADP-Ribosylation. *Mol. Cell*, 10.1016/j.molcel.2015.06.012.
32. Hottiger,M.O. (2015) Nuclear ADP-ribosylation and its role in chromatin plasticity, cell differentiation, and epigenetics. *Annu. Rev. Biochem.*, 10.1146/annurev-biochem-060614-034506.
33. Leslie Pedrioli,D.M., Leutert,M., Bilan,V., Nowak,K., Gunasekera,K., Ferrari,E., Imhof,R., Malmström,L. and Hottiger,M.O. (2018) Comprehensive ADP-ribosylome analysis identifies tyrosine as an ADP-ribose acceptor site. *EMBO Rep.*, 10.15252/embr.201745310.
34. Larsen,S.C., Hendriks,I.A., Lyon,D., Jensen,L.J. and Nielsen,M.L. (2018) Systems-wide Analysis of Serine ADP-Ribosylation Reveals Widespread Occurrence and Site-Specific Overlap with Phosphorylation. *Cell Rep.*, 10.1016/j.celrep.2018.07.083.
35. Zhang,Y., Wang,J., Ding,M. and Yu,Y. (2013) Site-specific characterization of the Asp-and Glu-ADP-ribosylated proteome. *Nat. Methods*, 10.1038/nmeth.2603.
36. Vivelo,C.A. and Leung,A.K.L. (2015) Proteomics approaches to identify mono-(ADP-ribosyl)ated and poly(ADP-ribosyl)ated proteins. *Proteomics*, 10.1002/pmic.201400217.
37. Estève,P.O., Hang,G.C., Smallwood,A., Feehery,G.R., Gangisetty,O., Karpf,A.R., Carey,M.F. and Pradhan,S. (2006) Direct interaction between DNMT1 and G9a coordinates DNA and histone methylation during replication. *Genes Dev.*, 10.1101/gad.1463706.
38. Estève,P.O., Chin,H.G., Benner,J., Feehery,G.R., Samaranayake,M., Horwitz,G.A., Jacobsen,S.E. and Pradhan,S. (2009) Regulation of DNMT1 stability through SET7-mediated lysine methylation in mammalian cells. *Proc. Natl. Acad. Sci. U. S. A.*, 10.1073/pnas.0810362106.

39. Chin,H.G., Esteve,P.O., Ruse,C., Lee,J., Schaus,S.E., Pradhan,S., Hansen,U. and de la Cruz,E.M. (2020) The microtubule-associated histone methyltransferase SET8, facilitated by transcription factor LSF, methylates α-tubulin. *J. Biol. Chem.*, 10.1074/jbc.RA119.010951.
40. Kim,G. Do, Ni,J., Kelesoglu,N., Roberts,R.J. and Pradhan,S. (2002) Co-operation and communication between the human maintenance and de novo DNA (cytosine-5) methyltransferases. *EMBO J.*, 10.1093/emboj/cdf401.
41. Patnaik,D., Hang,G.C., Estève,P.O., Benner,J., Jacobsen,S.E. and Pradhan,S. (2004) Substrate specificity and kinetic mechanism of mammalian G9a histone H3 methyltransferase. *J. Biol. Chem.*, 10.1074/jbc.M409604200.
42. Eng,J.K., McCormack,A.L. and Yates,J.R. (1994) An approach to correlate tandem mass spectral data of peptides with amino acid sequences in a protein database. *J. Am. Soc. Mass Spectrom.*, 10.1016/1044-0305(94)80016-2.
43. Ponnaluri,V.K.C., Zhang,G., Estève,P.O., Spracklin,G., Sian,S., Xu,S. yong, Benoukraf,T. and Pradhan,S. (2017) NicE-seq: High resolution open chromatin profiling. *Genome Biol.*, 10.1186/s13059-017-1247-6.
44. Chin,H.G., Sun,Z., Vishnu,U.S., Hao,P., Cejas,P., Spracklin,G., Estève,P.O., Xu,S.Y., Long,H.W. and Pradhan,S. (2020) Universal NicE-seq for high-resolution accessible chromatin profiling for formaldehyde-fixed and FFPE tissues. *Clin. Epigenetics*, 10.1186/s13148-020-00921-6.
45. Langmead,B. and Salzberg,S.L. (2012) Fast gapped-read alignment with Bowtie 2 - Supplemental Information. *Nat. Methods*.
46. Li,H., Handsaker,B., Wysoker,A., Fennell,T., Ruan,J., Homer,N., Marth,G., Abecasis,G. and Durbin,R. (2009) The Sequence Alignment/Map format and SAMtools. *Bioinformatics*, 10.1093/bioinformatics/btp352.
47. Tarasov,A., Vilella,A.J., Cuppen,E., Nijman,I.J. and Prins,P. (2015) Sambamba: Fast processing of NGS alignment formats. *Bioinformatics*, 10.1093/bioinformatics/btv098.
48. Zhang,Y., Liu,T., Meyer,C.A., Eeckhoute,J., Johnson,D.S., Bernstein,B.E., Nussbaum,C., Myers,R.M., Brown,M., Li,W., *et al.* (2008) Model-based analysis of ChIP-Seq (MACS). *Genome Biol.*, 10.1186/gb-2008-9-9-r137.
49. Ramírez,F., Ryan,D.P., Grüning,B., Bhardwaj,V., Kilpert,F., Richter,A.S., Heyne,S., Dündar,F. and Manke,T. (2016) deepTools2: a next generation web server for deep-sequencing data analysis. *Nucleic Acids Res.*, 10.1093/nar/gkw257.
50. Heinz,S., Benner,C., Spann,N., Bertolino,E., Lin,Y.C., Laslo,P., Cheng,J.X., Murre,C., Singh,H. and Glass,C.K. (2010) Simple Combinations of Lineage-Determining Transcription Factors Prime cis-Regulatory Elements Required for Macrophage and B Cell Identities. *Mol. Cell*, 10.1016/j.molcel.2010.05.004.

51. R Core Team. (2020) A Language and Environment for Statistical Computing. Available online: http://www.r-project.org. *R Found. Stat. Comput.*
52. Zhang,J., Lee,D., Dhiman,V., Jiang,P., Xu,J., McGillivray,P., Yang,H., Liu,J., Meyerson,W., Clarke,D., *et al.* (2020) An integrative ENCODE resource for cancer genomics. *Nat. Commun.*, 10.1038/s41467-020-14743-w.
53. Robinson,J.T., Thorvaldsdóttir,H., Winckler,W., Guttman,M., Lander,E.S., Getz,G. and Mesirov,J.P. (2011) Integrative genomics viewer. *Nat. Biotechnol.*, 10.1038/nbt.1754.
54. Ernst,J. and Kellis,M. (2012) ChromHMM: Automating chromatin-state discovery and characterization. *Nat. Methods*, 10.1038/nmeth.1906.
55. Dobin,A., Davis,C.A., Schlesinger,F., Drenkow,J., Zaleski,C., Jha,S., Batut,P., Chaisson,M. and Gingeras,T.R. (2013) STAR: Ultrafast universal RNA-seq aligner. *Bioinformatics*, 10.1093/bioinformatics/bts635.
56. Anders,S., Pyl,P.T. and Huber,W. (2015) HTSeq-A Python framework to work with high-throughput sequencing data. *Bioinformatics*, 10.1093/bioinformatics/btu638.
57. Love,M.I., Huber,W. and Anders,S. (2014) Moderated estimation of fold change and dispersion for RNA-seq data with DESeq2. *Genome Biol.*, 10.1186/s13059-014-0550-8.
58. Estève,P.O., Vishnu,U.S., Chin,H.G. and Pradhan,S. (2020) Visualization and Sequencing of Accessible Chromatin Reveals Cell Cycle and Post-HDAC inhibitor Treatment Dynamics. *J. Mol. Biol.*, 10.1016/j.jmb.2020.07.023.
59. Jørgensen,S., Elvers,I., Trelle,M.B., Menzel,T., Eskildsen,M., Jensen,O.N., Helleday,T., Helin,K. and Sørensen,C.S. (2007) The histone methyltransferase SET8 is required for S-phase progression. *J. Cell Biol.*, 10.1083/jcb.200706150.
60. An,Z., Chen,Y., Koomen,J.M. and Merkler,D.J. (2012) A mass spectrometry-based method to screen for α-amidated peptides. *Proteomics*, 10.1002/pmic.201100327.
61. Hengel,S.M., Shaffer,S.A., Nunn,B.L. and Goodlett,D.R. (2009) Tandem Mass Spectrometry Investigation of ADP-ribosylated Kemptide. *J. Am. Soc. Mass Spectrom.*, 10.1016/j.jasms.2008.10.025.
62. Huen,M.S.Y., Sy,S.M.H., Van Deursen,J.M. and Chen,J. (2008) Direct interaction between SET8 and proliferating cell nuclear antigen couples H4-K20 methylation with DNA replication. *J. Biol. Chem.*, 10.1074/jbc.C700242200.
63. Girish,T.S., McGinty,R.K. and Tan,S. (2016) Multivalent interactions by the set8 histone methyltransferase with its nucleosome substrate. *J. Mol. Biol.*, 10.1016/j.jmb.2016.02.025.
64. Wang,C., Qu,C., Alippe,Y., Bonar,S.L., Civitelli,R., Abu-Amer,Y., Hottiger,M.O. and Mbalaviele,G. (2016) Poly-ADP-ribosylation-mediated degradation of ARTD1 by the NLRP3 inflammasome is a prerequisite for osteoclast maturation. *Cell Death Dis.*, 10.1038/cddis.2016.58.

65. Hu,K., Wu,W., Li,Y., Lin,L., Chen,D., Yan,H., Xiao,X., Chen,H., Chen,Z., Zhang,Y., *et al.* (2019) Poly(ADP -ribosyl)ation of BRD 7 by PARP 1 confers resistance to DNA -damaging chemotherapeutic agents . *EMBO Rep.*, 10.15252/embr.201846166.
66. Wang,Y., Xu,Z.D., Mao,J.H., Hsieh,D., Au,A., Jablons,D.M., Li,H. and You,L. (2015) PR-Set7 is degraded in a conditional Cul4A transgenic mouse model of lung cancer. *Chinese J. Lung Cancer*, 10.3779/j.issn.1009-3419.2015.06.15.
67. Ke,Y., Han,Y., Guo,X., Wen,J., Wang,K., Jiang,X., Tian,X., Ba,X., Boldogh,I. and Zeng,X. (2017) PARP1 promotes gene expression at the post-transcriptiona level by modulating the RNA-binding protein HuR. *Nat. Commun.*, 10.1038/ncomms14632.
68. Wang,Y., Guo,Y., Tang,C., Han,X., Xu,M., Sun,J., Zhao,Y., Zhang,Y., Wang,M., Cao,X., *et al.* (2019) Developmental Cytoplasmic-to-Nuclear Translocation of RNA-Binding Protein HuR Is Required for Adult Neurogenesis. *Cell Rep.*, 10.1016/j.celrep.2019.10.127.
69. Krishnakumar,R. and Kraus,W.L. (2010) PARP-1 Regulates Chromatin Structure and Transcription through a KDM5B-Dependent Pathway. *Mol. Cell*, 10.1016/j.molcel.2010.08.014.
70. Kassner,I., Barandun,M., Fey,M., Rosenthal,F. and Hottiger,M.O. (2013) Crosstalk between SET7/9-dependent methylation and ARTD1-mediated ADP-ribosylation of histone H1.4. *Epigenetics and Chromatin*, 10.1186/1756-8935-6-1.
71. Le May,N., Iltis,I., Amé,J.C., Zhovmer,A., Biard,D., Egly,J.M., Schreiber,V. and Coin,F. (2012) Poly (ADP-Ribose) Glycohydrolase Regulates Retinoic Acid Receptor-Mediated Gene Expression. *Mol. Cell*, 10.1016/j.molcel.2012.09.021.
72. Guetg,C., Scheifele,F., Rosenthal,F., Hottiger,M.O. and Santoro,R. (2012) Inheritance of Silent rDNA Chromatin Is Mediated by PARP1 via Noncoding RNA. *Mol. Cell*, 10.1016/j.molcel.2012.01.024.
73. De Vos,M., El Ramy,R., Quénet,D., Wolf,P., Spada,F., Magroun,N., Babbio,F., Schreiber,V., Leonhardt,H., Bonapace,I.M., *et al.* (2014) Poly(ADP-ribose) polymerase 1 (parp1) associates with E3 ubiquitin-protein ligase UHRF1 and modulates UHRF1 biological functions. *J. Biol. Chem.*, 10.1074/jbc.M113.527424.
74. Caiafa,P., Guastafierro,T. and Zampieri,M. (2009) Epigenetics: poly(ADP-ribosyl)ation of PARP-1 regulates genomic methylation patterns. *FASEB J.*, 10.1096/fj.08-123265.
75. Kapoor-Vazirani,P. and Vertino,P.M. (2014) A dual role for the histone methyltransferase PR-SET7/SETD8 and histone H4 lysine 20 monomethylation in the local regulation of RNA polymerase II pausing. *J. Biol. Chem.*, 10.1074/jbc.M113.520783.

Figure legends

Figure 1: Colocalization, binding and poly ADP-ribosylation of SET8 by PARP1. (A) Co-immunoprecipitation of endogenous SET8 and PARP1 in HCT116 cells. Rabbit IgG (left lane) was used as a negative control. (B) Colocalization between FLAG-PARP1 (red), GFP-SET8 (green) and endogenous PCNA (pink) in COS-7 cells. DAPI (blue) represents the nuclear DNA content. (C) Mapping of domain interactions using GST-pulldown assays between SET8 domains (top, left) and full-length recombinant PARP1 protein and GST-pulldown assays between PARP1 domains and full-length recombinant SET8 protein (top, right). The PARP1 or SET8 binding were detected by western blotting using PARP1 antibody (middle, left) or SET8 antibody (middle, right) respectively. Ponceau stain gels (bottom) represent the amount of GST beads constructs used for the GST-pulldown assays. (D) *In vitro* detection of full-length recombinant SET8 ADP-ribosylation by full-length recombinant PARP1 by western blotting using anti-ADP ribose antibody (top). Ponceau stain gels (bottom) represent the amount of PARP1 and SET8 recombinant enzyme used for ADP-ribosylation assay (bottom). (E) Detection of SET8 lysines ADP-ribosylation using mass spectrometry analysis of SET8 ADP-ribosylated peptides by full-length recombinant PARP1 protein *in vitro*.

Figure 2: Poly ADP-ribosylation impairs DNA, nucleosome binding and catalytic activity of SET8 protein. (A) Detection of unbound 100 bp DNA ladder by TBE ethidium bromide-stained gel in supernatants (left lane) on GST-SET8 domains or mutant (M) using GST-pulldown assays (top, left side). Asterisks are representing shift of DNA on GST-SET8 157-352 amino acid protein or GST-SET8 full-length protein (FL) beads. Ponceau stain represents the amount of GST beads constructs used for the GST-pulldown (bottom, left side). (B) Different concentrations of recombinant full-length SET8 protein binding to DNA using EMSA to determine the equilibrium dissociation constant (Kd). (C) Detection of unbound mononucleosome by TBE ethidium bromide-stained gel in supernatants on GST beads versus GST-SET8 domains or mutant (M) beads using GST-pulldown assays. (D) Detection of unbound DNA (left side) or unbound mononucleosome (right side) by TBE ethidium bromide-stained gel in supernatants (top) on GST beads versus GST-SET8 FL beads using GST-pulldown assays. GST or GST-SET8 FL beads were poly ADP-ribosylated or not (with or without NAD) using full-length recombinant PARP1 as demonstrated by western blot using anti-ADP ribose antibody (middle). Ponceau stain gel (bottom) represents the amount of GST bead constructs used for the GST-pulldown and the ADP-ribosylation western blot analysis. (E) SET8 histone methyltransferase assay on full-length recombinant histone H4 using full-length recombinant SET8 in presence or absence of activated full-length recombinant PARP1.

Figure 3: PARP1 promotes SET8 protein degradation. (A) GFP-SET8 immunoprecipitation in overexpressed GFP-SET8 COS-7 cells with or without FLAG-PARP1 overexpression in presence or

not of the proteasome inhibitor MG132. Western blots detecting the amount of GFP-SET8 protein overexpressed in total extract (top, left) as well as the amount of FLAG-PARP1 protein overexpressed (top, right) using anti-GFP and anti-FLAG antibody respectively. Western blots detecting the amount of ubiquitin (Ub) (bottom, left) or ADP-ribosylation (bottom, right) of immunoprecipitated GFP-SET8 protein using anti-HA and anti-ADP ribose antibody respectively. Anti-actin was used as a loading control (middle). (B) GFP-SET8 immunoprecipitation in overexpressed GFP-SET8 COS-7 cells in presence or not (DMSO) of Cullin inhibitor (Cul4Ai) or PARG inhibitor (PARGi). Western blot detection of total GFP-SET8 protein levels overexpressed in COS-7 cells (top). Anti-actin antibody was used as control (middle). Western blot detecting the amount of poly-ADP ribosylation (bottom) of immunoprecipitated GFP-SET8 protein using an anti-ADP ribose antibody. (C) Western blots (left side) detecting the amount of PARP1 (top), SET8 protein (middle) as well as the amount of H4K20me1, H4K20me2 and H4K20me3 levels (bottom) in total protein extract of knockdown HeLa cells treated with esiRNA GFP (control), esiRNA PARP1 and esiRNA SET8, respectively. Respective densitometry analyses of protein abundance representative of at least 2 biological experiments are shown (right side). Ponceau stain was used as control (left side).

Figure 4: Cell cycle dependent interaction of PARP1 and SET8 correlates with global H4K20me1. (A) Western blot indicating PARP1 (top, left), SET8 (middle, left) and H4K20me1 (middle, left) levels in total protein extracts from HeLa cells synchronized in G1, S and G2/M phases, respectively. Western blot of CDT1 protein levels is shown as a cell cycle synchronization control as well as Ponceau stain for loading control and densitometry analyses (bottom, left). Respective densitometry analyses of H4K20me1 (top, right) and SET8 (bottom, right) relative protein abundances are shown (right) and representative of at least 2 biological experiments. (B) SET8 immunoprecipitation from total protein extract in HeLa cells synchronized in G1, S and G2/M phases. Western blots detection of PARP1 (top, left) as well as SET8 immunoprecipitated protein levels (bottom, left) are revealed. Densitometry analyses of PARP1/SET8 ratio during G1, S and G2/M cell cycle phases are shown (right) and are representative of at least 2 biological experiments. (C) Pulsed chased cells with 5-ethynyl-2-deoxyuridine (EdU) to label DNA (magenta) is transfected with GFP-SET8 (green). Endogenous ADP-ribose (red) is revealed by anti-ADP-ribose conjugated with Texas Red. Merged images demonstrates the co-localization of EDU, SET8 and ADP-ribose.

Figure 5: PARP1 regulates H4K20me1 distribution in the genome. (A) Genome-wide metagene plot showing H4K20me1 profile (ChIP-seq) in the human (hg38) genes with ± 2Kb of flanking region following Transcription start site (TSS) and Transcription end site (TES) in PARP1 overexpressed HeLa cells and its control. (B) Metagene plot of PARP1 knockdown cells and its control. (C) Spearman correlation of H4K20me1 regions in the human (hg38) genes and open

chromatin region in PARP1 overexpressed HeLa cells and its control. (D) Spearman correlation of H4K20me1 regions in the human (hg38) genes and open chromatin region in PARP1 knockdown cells and its control. (E) Spearman correlation of H4K20me1 regions in the human (hg38) genes and RNA expression in PARP1 overexpressed HeLa cells and its control. (F) Spearman correlation of H4K20me1 regions in the human (hg38) genes and RNA expression in PARP1 knockdown cells and its control. (G) Peak width profile of H4K20me1 by binning the peaks into different lengths in PARP1 overexpressed HeLa cells and its control (top panel) and PARP1 knockdown cells and its control (bottom panel) showing gain and loss in peak width. (H) Representative IGV genomic tracks showing H4K20me1 regions and respective RNA expression profile in PARP1 knockdown cells and its control. (I) Representative IGV genomic tracks showing H4K20me1 regions and respective RNA expression profile in PARP1 overexpressed HeLa cells and its control.

Supplementary figures

Figure S1: Predicted SET8 structure and mutational analysis of PARP1 binding. (A) Schematic presentation of SET8 and its domains on the top followed by predicted structural ordered and disorder regions of the enzyme using PONDR score. (B) Predicted folded, unfolded, hydrophobic and charge region fold index of SET8 using PLAAC algorithm. (C) GST pull down of GST-SET8FL or GST-SET8mut (K86A, K158/159A, K162/164A, R168A, K169/170A, K174A) of PARP1 full-length enzyme. Western blot probed with anti-PARP1 antibody (top, left), and the relative pulldown of PARP1 quantitated and shown in arbitrary unit (top, right). Loading of the exact blot shown using ponceau staining (bottom).

Figure S2: Detail poly ADP-ribosylation mapping of SET8. (A) Full length SET8 is poly ADP ribosylated by PARP1. The enzymatic in vitro reaction was separated using SDS-PAGE, western blotted and probed with anti-PAR antibody. The shifted SET8 band shows the ADP ribosylated SET8 (top). Loading of the exact blot shown using ponceau staining (bottom). (B) ADP-ribosylation of various SET8 domain in the presence of PARP1. The ribosylated SET8 GST-SET8 N-t (1-98), GST-SET8 DD (157-352) domains as well as GST-SET8 FL are shown by western blotting using anti-PAR antibody (top). Loading of the exact blot shown using ponceau staining (bottom). (C) ADP-ribosylation of various GST-SET8 regions in the presence of PARP1. GST-SET8 N-t (1-98), GST-SET8 DD (157-352) and GST-SET8 FL show ribosylation (top). Loading of the exact blot shown using ponceau staining (bottom). (D) Detailed ADP-ribosylation analysis of various truncated SET8 regions between amino acids 130-352 in the presence of PARP1. GST-SET8 (130-152), GST-SET8 (157-352), GST-SET8 (170-352) as well as GST-SET8 FL shows ADP-ribosylation (top). Loading of the exact blot shown using ponceau staining (bottom).

Figure S3: Characterization of ADP-ribosylation of SET8 synthetic peptide KPLAGIYRKREEK-NH2 using high resolution mass spectrometry and isotope quantification in nanoLC.

(A) Quantification of peptide KPLAGIYRKREEK-NH2 (charge +3) at four time points: 0 min (negative control), 1hr, 4rhs and overnight (ON) reaction with PARP1. Peak areas were determined with SIEVE software package for the three main isotopes m/z 529.65449, m/z 529.98877 and m/z 530.32300, theoretical values determined with Protein Prospector MS Isotope. The figure displays the measured isotopes 0, 1 and 2 with Orbitrap MS. (B) Quantification of peptide (ADPr)KPLAGIYRKREEK-NH2 (charge +3) at four time points: 0 min (negative control), 1hr, 4rhs and overnight (ON) reaction with PARP1. Peak areas were determined with SIEVE software package for the three main isotopes m/z 710.00819, m/z 710.34247 and m/z 710.67670, theoretical values determined with Protein Prospector MS Isotope. The figure displays the measured isotopes 0, 1 and 2 with Orbitrap MS. (C) Quantification of peptide (ADPr)KPLAGIYRKREEK-NH2 (charge +4) at four time points: 0 min (negative control), 1hr, 4rhs and overnight (ON) reaction with PARP1. Peak areas were

determined with SIEVE software package for the three main isotopes m/z 532.75796, m/z 533.00867 and m/z 533.25934, theoretical values determined with Protein Prospector MS Isotope. The figure displays the measured isotopes 0, 1 and 2 with Orbitrap MS. (D) Chromatographic profile of the main isotopes of (1ADPr) KPLAGIYRKREEK-NH2 and (2ADPr) KPLAGIYRKREEK-NH2 detected at 5 min reaction with PARP1. (E) Chromatographic profile of the main isotopes of (1ADPr) KPLAGIYRKREEK-NH2 and (2ADPr) KPLAGIYRKREEK-NH2 detected at 15 min reaction with PARP1.

Figure S4. Characterization of ADP-ribosylation of SET8 synthetic peptide KPLAGIYRKREEK-NH2 using high resolution/high accuracy MS/MS HCD fragmentation, [M+3H]3+ precursor m/z 710.00 and [M+4H]4+ precursor m/z 532.75. (A) Characteristics ADP-ribose modification fragmentation ions (m-ions peptide free modification fragment ions):m1= 136.1, m3=250, m5=348, m8=428 (top panel). Ion m/z 136.1 could be sourced from either tyrosine immonium ion (m/z 136.0762) or [adenine+H]+ (m/z 136.0623). Fragment ions with intact peptide p1 and intact peptide with ribose phosphate p5 are shown on the bottom panel, m/z 500 - 900. The nomenclature for ADP-ribosylation fragment ions is according to (Hengel et al, 2009). Inset shows the [M+3H]3+ precursor full scan MS spectrum. **(**B) Similar to charge state +3, fragmented precursor charge state +4 showed characteristics ADP-ribose modification fragment ions. Increased intensity sequencing ions are present in the bottom panel, m/z 500 - 900. Inset shows the [M+4H]4+ precursor full scan MS spectrum.

Figure S5. Characterization of ADP-ribosylation of SET8 synthetic peptide KPLAGIYRKREEK-NH2 using MS/MS CID fragmentation. [M+3H]3+ precursor m/z 710.008 and [M+4H]4+ precursor m/z 532.75 are shown. Scoring of ion propensity matches of the ADPr unit relative to seven possible amino acid locations in CID MS/MS spectra of (ADPr)KPLAGIYRKREEK-NH2.

Figure S6. Characterization of ADP-ribosylation of SET8 synthetic peptide KKPIKGKQAPRKK-NH2 using high resolution mass spectrometry and isotope quantification in nanoLC. (A) Quantification of peptide KKPIKGKQAPRKK-NH2 (charge +3) at four time points: 0 min (negative control), 1hr, 4 hrs and overnight (ON) reaction with PARP1. Peak areas were determined with SIEVE software package for the three main isotopes m/z 502.67534, m/z 503.00960 and m/z 503.34383, theoretical values determined with Protein Prospector MS Isotope. The figure displays the measured isotopes 0, 1 and 2 with Orbitrap MS. (B) Quantification of peptide (ADPr)KKPIKGKQAPRKK-NH2 (charge +4) at four time points: 0 min (negative control), 1hr, 4 hrs and overnight (ON) reaction with PARP1. Peak areas were determined with SIEVE software package for the three main isotopes m/z 512.52360, m/z 512.77430 and m/z 513.02497, theoretical values determined with Protein Prospector MS Isotope. The figure displays the measured isotopes 0, 1 and 2 with Orbitrap MS.

Figure S7. Characterization of ADP-ribosylation of SET8 synthetic peptide KKPIKGKQAPRKK-NH2 using MS/MS CID fragmentation, [M+4H]4+ precursor m/z 512.52. Characteristics ADP-ribose modification fragmentation ions (m-ions peptide free modification fragment ions): m5=348 and m8=428 (top panel). Fragment peptide ions are present most probably due to neutral loss of ADP-ribose fragments, within the unit resolution on linear ion trap MS/MS spectra (bottom panel). Inset shows the [M+4H]4+ precursor full scan MS spectrum.

Figure S8: DNA enhances SET8 and PARP1 binding. (A) GST pull down assay of GST-SET8 FL with PARP1 full length in the presence or absence of DNase I. Western blot using anti-PARP1 antibody revels the presence of PARP1 (top, left side). The relative pulldown of PARP1 quantitated and shown in arbitrary unit (right side). Loading of the exact blot shown using ponceau staining (bottom, left side).

Figure S9: PARP1 overexpression leads to change the cellular levels of H4K20 methylation. (A) Equal amounts of cell extract from cells transfected with FLAG or FLAG-PARP1, blotted and probed with antibodies as indicated. Equal loading is shown by ponceau staining. (B) Western blot showing levels of mono, di, tri methylation of H4K20 and SET8. Relative amounts of protein are measured by scanning three independent blots.

Figure S10: Genomic analysis of PARP1 overexpression and depletion. Pearson correlation of H4K20me1 regions in (A) PARP1 overexpressed HeLa cells and its control. (B) PARP1 knockdown cells and its control. (C) Peak annotation showing genomic representation of H4K20me1 in PARP1 overexpressed HeLa cells and its control (left panel) and PARP1 knockdown cells and its control (right panel). (D) Peak annotation showing repeat elements profile in PARP1 overexpressed HeLa cells and its control (top panel) and PARP1 knockdown cells and its control (bottom panel).

Figure S11: Genomic analysis of PARP1 overexpression and depletion. (A) Genome-wide metagene plot showing open chromatin profile (NicE-seq) in the human (hg38) genes with ± 2Kb of flanking region following Transcription start site (TSS) and Transcription end site (TES) in PARP1 overexpressed HeLa cells and its control (B) Similar to A with PARP1 knockdown cells and its control. (C) Pie chart representation of H4K20me1 bound differentially expressed genes in PARP1 overexpressed HeLa cells and its control. (D) Similar pie chart for PARP1 knockdown cells and its control. (E) Histone mark probabilities in different chromatin states in PARP1 overexpressed HeLa cells and its control, and (F) PARP1 knockdown cells and its control.

Figure S12: Transcription factor binding site analysis. Heatmap representing the enrichment of consensus TF-binding motifs identified from H4K20me1 ChIP-seq in (A) PARP1 overexpressed HeLa cells and its control. (B) PARP1 knockdown cells and its control.

Table S1: Proteomic analysis of SET8 pull-down in HEK293T cells using LC-MS.

Table S2A: Up and down regulated genes post PARP1 overexpression.

Table S2B: Up and down regulated genes post PARP1 knock down.

Table S3A: Wnt signaling pathway associated TFs enriched due to PARP1 overexpression.

Table S3B: Wnt signaling pathway associated TFs enriched due to PARP1 knock down.

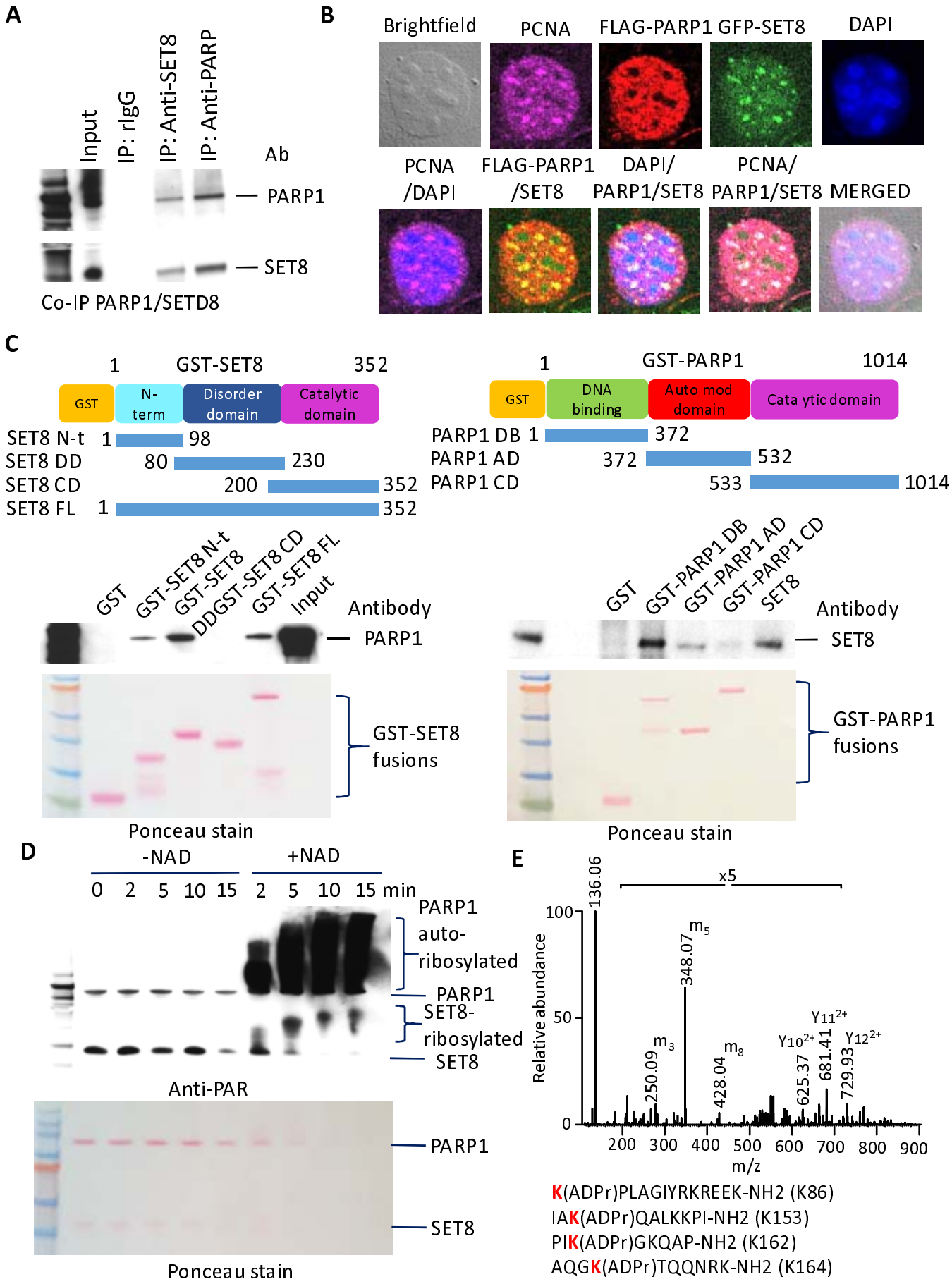
A
Input
IP: rIgG
IP: Anti-SET8
IP: Anti-PARP
Ab
PARP1
SET8
Co-IP PARP1/SETD8
B
Brightfield
PCNA
FLAG-PARP1
GFP-SET8
DAPI
PCNA /DAPI
FLAG-PARP1 /SET8
DAPI/ PARP1/SET8
PCNA/ PARP1/SET8
MERGED
C
1
GST-SET8
352
GST
N-term
Disorder domain
Catalytic domain
SET8 N-t 1 98
SET8 DD 80 230
SET8 CD 200 352
SET8 FL 1 352
1
GST-PARP1
1014
GST
DNA binding
Auto mod domain
Catalytic domain
PARP1 DB 1 372
PARP1 AD 372 532
PARP1 CD 533 1014
GST
GST-SET8 N-t
GST-SET8
DDGST-SET8 CD
GST-SET8 FL
Input
Antibody
PARP1
GST-SET8 fusions
Ponceau stain
GST
GST-PARP1 DB
GST-PARP1 AD
GST-PARP1 CD
SET8
Antibody
SET8
GST-PARP1 fusions
Ponceau stain
D
-NAD
+NAD
0 2 5 10 15 2 5 10 15 min
PARP1 auto-ribosylated
PARP1
SET8-ribosylated
SET8
Anti-PAR
PARP1
SET8
Ponceau stain
E
136.06
x5
100
50
0
Relative abundance
m5
348.07
m3
250.09
m8
428.04
Y10 2+
625.37
Y11 2+
681.41
Y12 2+
729.93
200 300 400 500 600 700 800 900
m/z
K(ADPr)PLAGIYRKREEK-NH2 (K86)
IAK(ADPr)QALKKPI-NH2 (K153)
PIK(ADPr)GKQAP-NH2 (K162)
AQGK(ADPr)TQQNRK-NH2 (K164)

Fig. 1

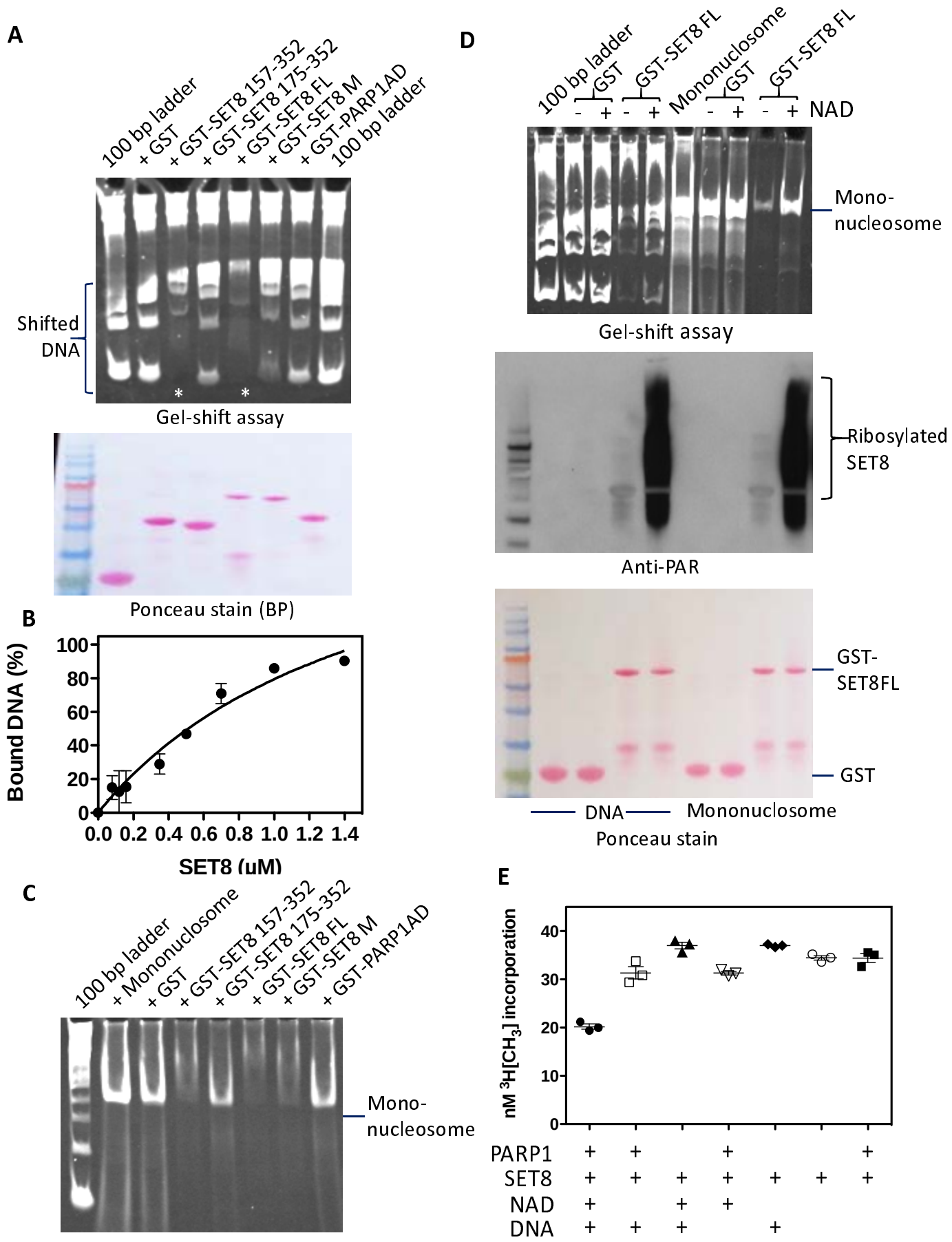
A
100 bp ladder
+ GST
+ GST-SET8 157-352
+ GST-SET8 175-352
+ GST-SET8 FL
+ GST-SET8 M
+ GST-PARP1AD
100 bp ladder
Shifted DNA
Gel-shift assay
Ponceau stain (BP)
B
Bound DNA (%)
SET8 (uM)
C
100 bp ladder
+ Mononucleosome
+ GST
+ GST-SET8 157-352
+ GST-SET8 175-352
+ GST-SET8 FL
+ GST-SET8 M
+ GST-PARP1AD
Mono-nucleosome
D
100 bp ladder
GST
GST-SET8 FL
Mononucleosome
GST
GST-SET8 FL
NAD
Mono-nucleosome
Gel-shift assay
Ribosylated SET8
Anti-PAR
GST-SET8FL
GST
DNA
Mononucleosome
Ponceau stain
E
nM ^{3}H[CH$_3$] incorporation
PARP1
SET8
NAD
DNA

Fig. 2

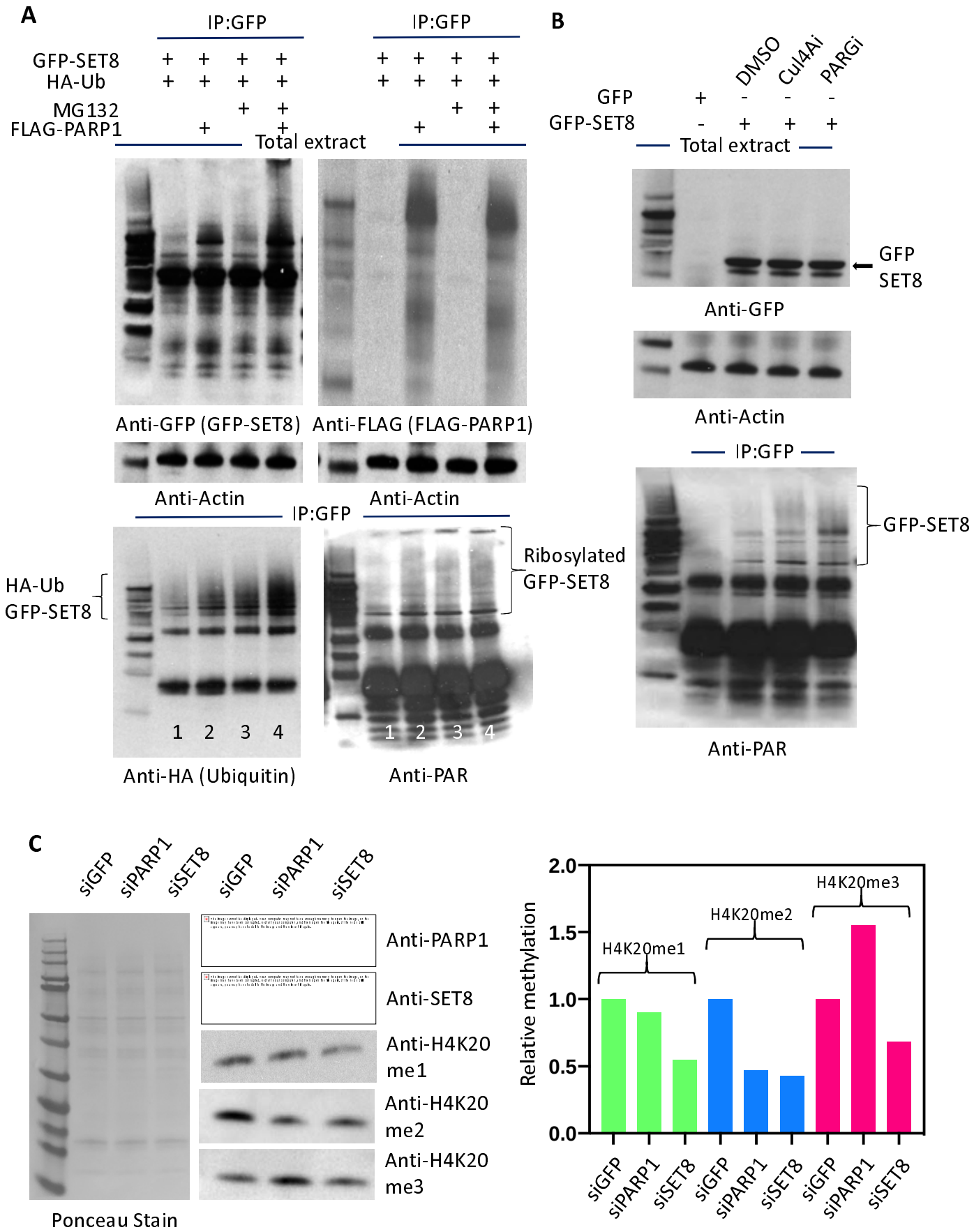
A
IP:GFP
IP:GFP
GFP-SET8
HA-Ub
MG132
FLAG-PARP1
Total extract
Anti-GFP (GFP-SET8)
Anti-FLAG (FLAG-PARP1)
Anti-Actin
Anti-Actin
IP:GFP
HA-Ub
GFP-SET8
Ribosylated
GFP-SET8
1 2 3 4
1 2 3 4
Anti-HA (Ubiquitin)
Anti-PAR
B
DMSO
Cul4Ai
PARGi
GFP
GFP-SET8
Total extract
GFP
SET8
Anti-GFP
Anti-Actin
IP:GFP
GFP-SET8
Anti-PAR
C
siGFP
siPARP1
siSET8
siGFP
siPARP1
siSET8
Anti-PARP1
Anti-SET8
Anti-H4K20 me1
Anti-H4K20 me2
Anti-H4K20 me3
Ponceau Stain
Relative methylation
2.0
1.5
1.0
0.5
0.0
H4K20me1
H4K20me2
H4K20me3
siGFP
siPARP1
siSET8
siGFP
siPARP1
siSET8
siGFP
siPARP1
siSET8

Fig. 3

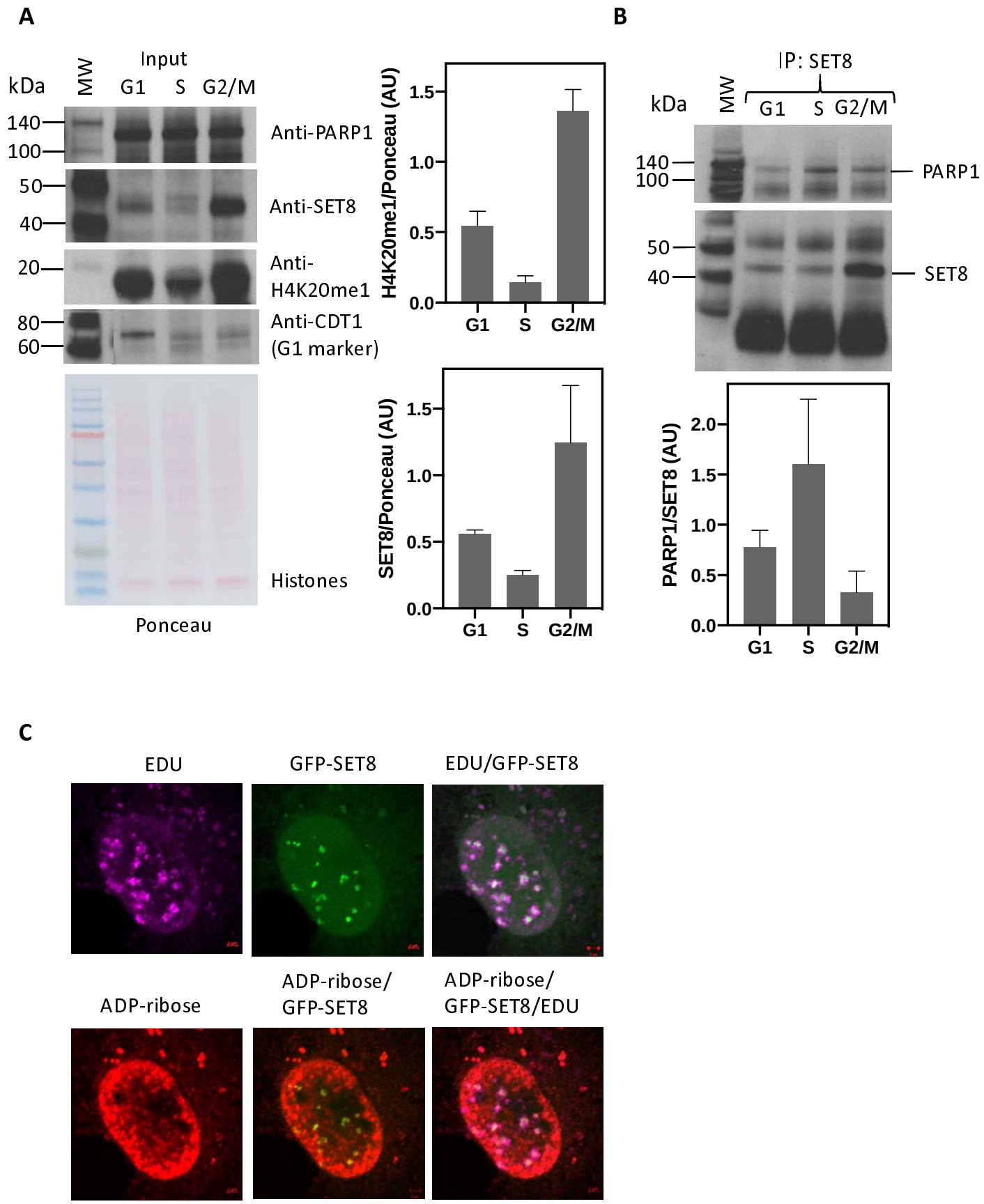
A
Input
kDa
MW
G1
S
G2/M
140
100
50
40
20
80
60
Anti-PARP1
Anti-SET8
Anti-H4K20me1
Anti-CDT1
(G1 marker)
Histones
Ponceau
H4K20me1/Ponceau (AU)
SET8/Ponceau (AU)
B
IP: SET8
PARP1
SET8
PARP1/SET8 (AU)
C
EDU
GFP-SET8
EDU/GFP-SET8
ADP-ribose
ADP-ribose/
GFP-SET8
ADP-ribose/
GFP-SET8/EDU

Fig. 4

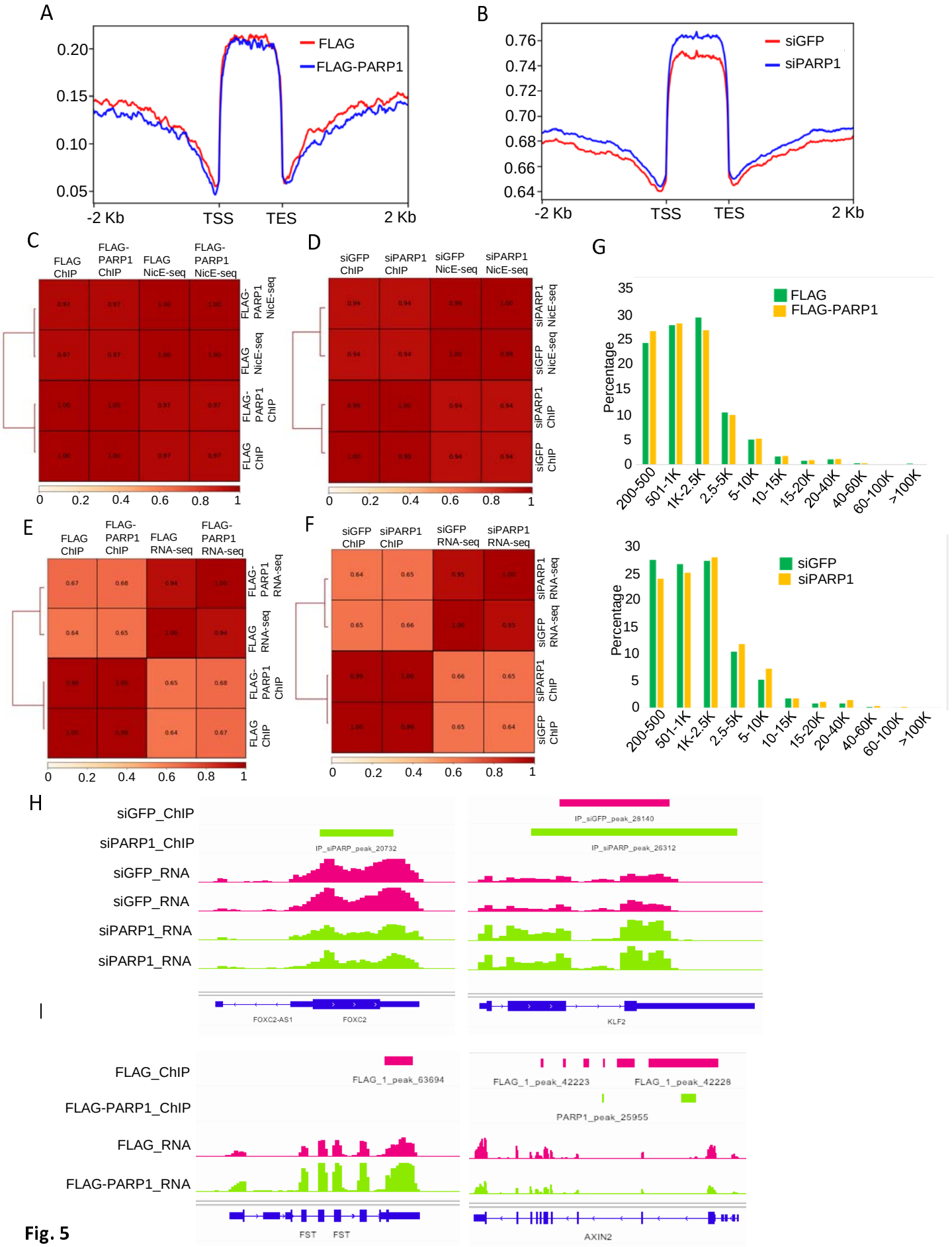
A
FLAG
FLAG-PARP1
0.20
0.15
0.10
0.05
-2 Kb
TSS
TES
2 Kb
B
siGFP
siPARP1
0.76
0.74
0.72
0.70
0.68
0.66
0.64
-2 Kb
TSS
TES
2 Kb
C
FLAG ChIP
FLAG-PARP1 ChIP
FLAG NicE-seq
FLAG-PARP1 NicE-seq
D
siGFP ChIP
siPARP1 ChIP
siGFP NicE-seq
siPARP1 NicE-seq
G
FLAG
FLAG-PARP1
Percentage
200-500
501-1K
1K-2.5K
2.5-5K
5-10K
10-15K
15-20K
20-40K
40-60K
60-100K
>100K
E
FLAG ChIP
FLAG-PARP1 ChIP
FLAG RNA-seq
FLAG-PARP1 RNA-seq
F
siGFP ChIP
siPARP1 ChIP
siGFP RNA-seq
siPARP1 RNA-seq
siGFP
siPARP1
H
siGFP_ChIP
siPARP1_ChIP
siGFP_RNA
siGFP_RNA
siPARP1_RNA
siPARP1_RNA
IP_siGFP_peak_28140
IP_siPARP_peak_20732
IP_siPARP_peak_26312
FOXC2-AS1
FOXC2
KLF2
I
FLAG_ChIP
FLAG-PARP1_ChIP
FLAG_RNA
FLAG-PARP1_RNA
FLAG_1_peak_63694
FLAG_1_peak_42223
FLAG_1_peak_42228
PARP1_peak_25955
FST
FST
AXIN2

Fig. 5